学位論文

Mesothelial cells with mesenchymal features enhance peritoneal dissemination by forming a protumorigenic microenvironment

（間葉系の特徴を有する中皮細胞は腫瘍促進性の微小環境を形成することで腹膜播種を進展する）

米村　敦子

Atsuko　Yonemura

熊本大学大学院医学教育部博士課程医学専攻消化器外科学

指導教員

馬場　秀夫　教授

熊本大学大学院医学教育部博士課程医学専攻消化器外科学

2023 年 3 月

学　位　論　文

論文題名　：　**Mesothelial cells with mesenchymal features enhance peritoneal dissemination by forming a protumorigenic microenvironment**
（間葉系の特徴を有する中皮細胞は腫瘍促進性の微小環境を形成することで腹膜播種を進展する）

著 者 名　：　米　村　敦　子
Atsuko　Yonemura

指導教員名　：　熊本大学大学院医学教育部博士課程医学専攻消化器外科学
馬　場　秀　夫　教授

審査委員名　：　消化器内科学担当教授　田　中　靖　人
産科婦人科学担当教授　近　藤　英　治
細胞医学担当教授　中　尾　光　善

2023 年 3 月

Cell Reports

Article

Mesothelial cells with mesenchymal features enhance peritoneal dissemination by forming a protumorigenic microenvironment

Graphical abstract

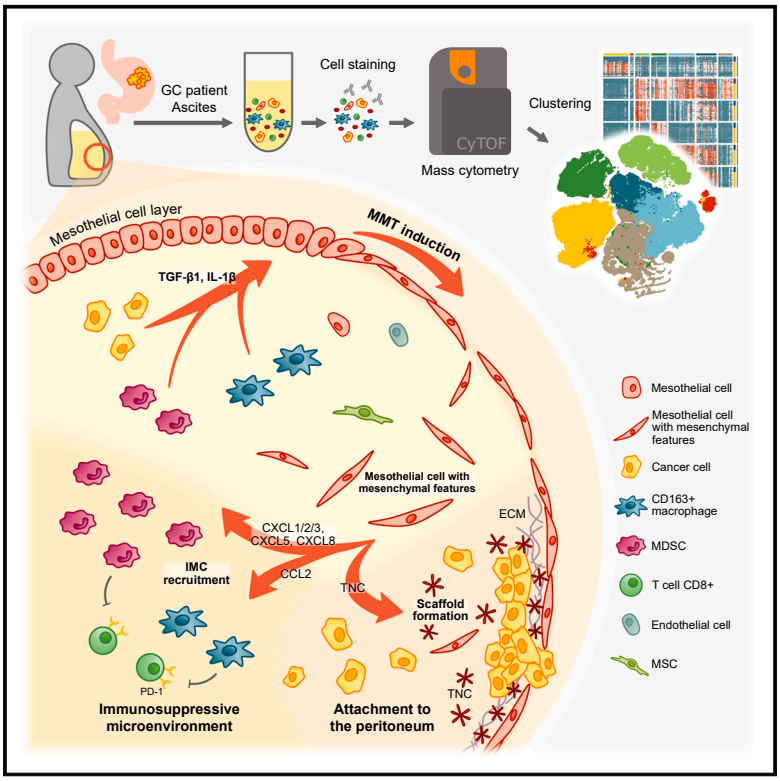

Highlights

- Mesenchymal cells diversity exists in malignant ascites of patients with GC
- An immunosuppressive microenvironment is formed in malignant ascites of patients with GC
- MMT-induced mesothelial cells produce chemokines involved in IMC recruitment
- TNC derived from MMT-induced mesothelial cells enhances metastatic colonization

Authors

Atsuko Yonemura, Takashi Semba, Jun Zhang, ..., Hideo Baba, Jaffer A. Ajani, Takatsugu Ishimoto

Correspondence

jajani@mdanderson.org (J.A.A.), takatsugu.ishimoto@jfcr.or.jp (T.I.)

In brief

Yonemura et al. showed that mesothelial cells with mesenchymal features are responsible for the immunosuppressive microenvironment in malignant ascites. MMT-induced mesothelial cells produce chemokines involved in IMC recruitment and enhance attachment to the peritoneum through TNC production as a scaffold for GC cells, leading to enhanced peritoneal dissemination.

Yonemura et al., 2024, Cell Reports *43*, 113613
January 23, 2024
https://doi.org/10.1016/j.celrep.2023.113613

CellPress

Cell Reports

CellPress
OPEN ACCESS

Article

Mesothelial cells with mesenchymal features enhance peritoneal dissemination by forming a protumorigenic microenvironment

Atsuko Yonemura,[1,2,3] Takashi Semba,[2,3] Jun Zhang,[1,2,3] Yibo Fan,[4] Noriko Yasuda-Yoshihara,[1,2] Huaitao Wang,[1,2,3] Tomoyuki Uchihara,[1,2] Tadahito Yasuda,[1,2] Akiho Nishimura,[2,3] Lingfeng Fu,[1,2,3] Xichen Hu,[1,2,3] Feng Wei,[1,2] Fumimasa Kitamura,[1,2] Takahiko Akiyama,[1,2] Kohei Yamashita,[1] Kojiro Eto,[1] Shiro Iwagami,[1] Masaaki Iwatsuki,[1] Yuji Miyamoto,[1] Keisuke Matsusaki,[5] Juntaro Yamasaki,[6,7] Osamu Nagano,[6,7] Hideyuki Saya,[6,7] Shumei Song,[4] Patrick Tan,[8] Hideo Baba,[1,9] Jaffer A. Ajani,[4,*] and Takatsugu Ishimoto[1,2,3,10,*]

[1]Department of Gastroenterological Surgery, Graduate School of Medical Sciences, Kumamoto University, Kumamoto 860-8556, Japan
[2]Gastrointestinal Cancer Biology, International Research Center of Medical Sciences (IRCMS), Kumamoto University, Kumamoto 860-0811, Japan
[3]Division of Carcinogenesis, The Cancer Institute, Japanese Foundation for Cancer Research, Tokyo 135-8550, Japan
[4]Department of Gastrointestinal Medical Oncology, The University of Texas MD Anderson Cancer Center, Houston, TX 77030, USA
[5]Ascites Treatment Center, Kanamecho Hospital, Tokyo 171-0043, Japan
[6]Division of Gene Regulation, Institute for Advanced Medical Research, School of Medicine, Keio University, Tokyo 160-8582, Japan
[7]Division of Gene Regulation, Cancer Center, Fujita Health University, Toyoake 470-1192, Japan
[8]Program in Cancer and Stem Cell Biology, Duke-NUS Medical School, Singapore 169857, Singapore
[9]Center for Metabolic Regulation of Healthy Aging, Faculty of Life Sciences, Kumamoto University, Kumamoto 860-8556, Japan
[10]Lead contact
*Correspondence: jajani@mdanderson.org (J.A.A.), takatsugu.ishimoto@jfcr.or.jp (T.I.)
https://doi.org/10.1016/j.celrep.2023.113613

SUMMARY

Malignant ascites accompanied by peritoneal dissemination contain various factors and cell populations as well as cancer cells; however, how the tumor microenvironment is shaped in ascites remains unclear. Single-cell proteomic profiling and a comprehensive proteomic analysis are conducted to comprehensively characterize malignant ascites. Here, we find defects in immune effectors along with immunosuppressive cell accumulation in ascites of patients with gastric cancer (GC) and identify five distinct subpopulations of CD45(−)/EpCAM(−) cells. Mesothelial cells with mesenchymal features in CD45(−)/EpCAM(−) cells are the predominant source of chemokines involved in immunosuppressive myeloid cell (IMC) recruitment. Moreover, mesothelial-mesenchymal transition (MMT)-induced mesothelial cells strongly express extracellular matrix (ECM)-related genes, including tenascin-C (TNC), enhancing metastatic colonization. These findings highlight the definite roles of the mesenchymal cell population in the development of a protumorigenic microenvironment to promote peritoneal dissemination.

INTRODUCTION

Gastric cancer (GC) is the fifth most common cancer in terms of incidence and the third leading cause of cancer-related death worldwide.[1] GCs are divided into two subtypes according to Lauren's classification: intestinal-type GCs (IGCs) and diffuse-type GCs (DGCs).[2] DGCs are characterized by rapid progression and abundant stroma and are likely to show peritoneal dissemination. The accumulation of malignant ascites is frequently detected in patients with DGC with peritoneal dissemination. Although novel treatment options, including immune checkpoint inhibitors, have been developed and approved for advanced GC, the response rate of patients with GC with peritoneal dissemination is still limited.

For the development of peritoneal dissemination from primary GC in the stomach, GC cells need to survive in the peritoneal cavity after penetrating the gastric wall, attach to the peritoneum, and form tumors. Recent studies using whole-genome sequencing and transcriptome analyses of purified tumor cells from malignant ascites detected unique driver gene alterations and an epithelial-mesenchymal transition (EMT) phenotype in tumor cells purified from ascites.[1,3] High-resolution imaging analysis of clinical tumor samples across various histologies revealed that the phenotypic plasticity conferred to cancer cells by EMT allows adaptation to cytotoxic or molecular targeted therapy and could create a form of acquired transient drug resistance.[4] Additionally, integrated molecular profiling in a phase 2 trial of patients with metastatic GC treated with pembrolizumab (anti-PD-1 antibody) monotherapy showed that patients with GC with an EMT signature exhibited a poor response to this drug.[2]

Although unique characteristics such as EMT in ascitic GC cells have an impact on the survival advantage and the treatment

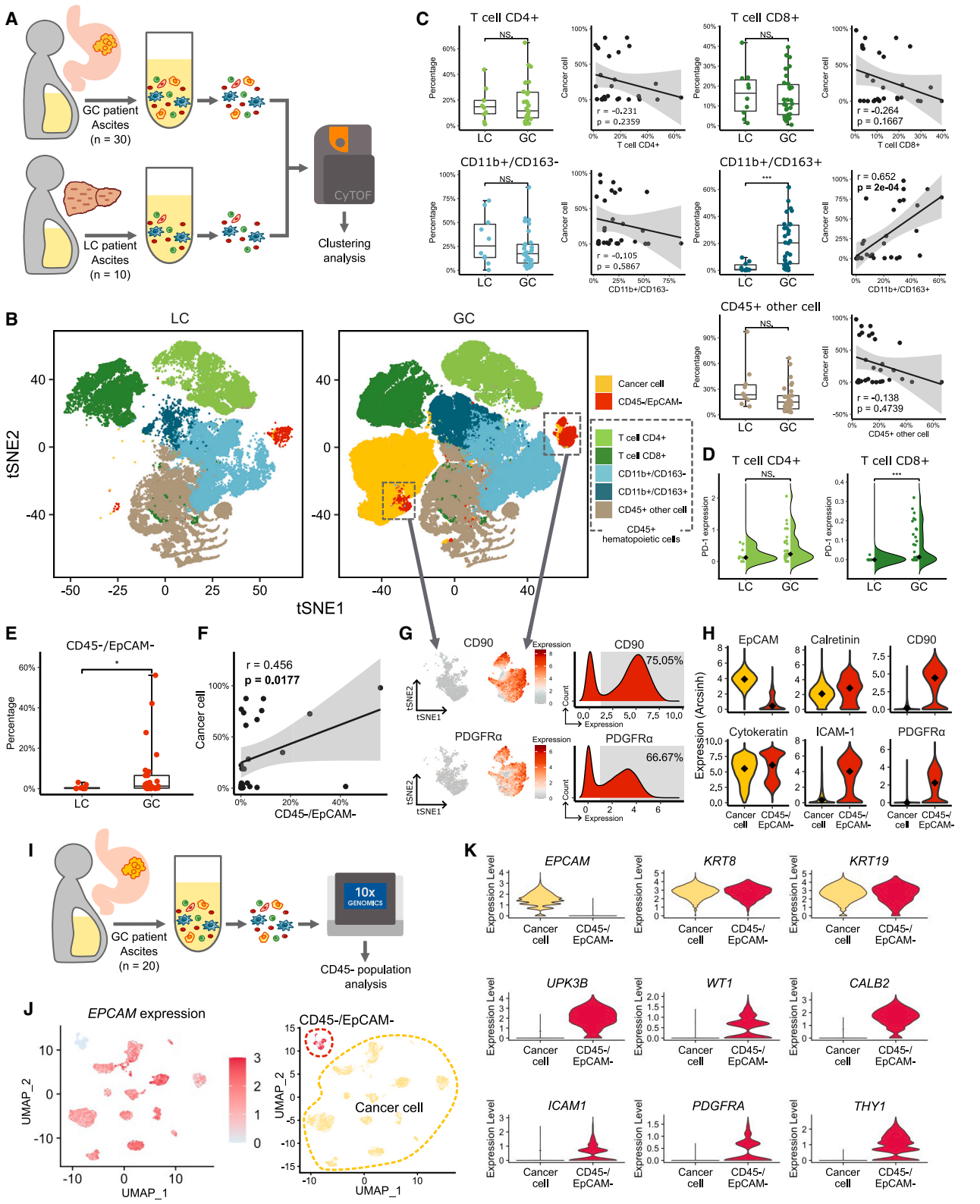

(legend on next page)

response, accumulating evidence has shown that the tumor microenvironment and soluble signals could affect the molecular features of cancer cells.[5,6] Therefore, peritoneal dissemination could be enhanced by nonmalignant cells, in addition to the invasive characteristics of the cancer cells themselves. Various types of cells coexist and interact with each other through cell-cell communication and secreted factors in malignant ascites. However, the cellular composition in malignant ascites and the role of nonmalignant cells in peritoneal dissemination have not been determined.

In the current study, we performed single-cell proteomic analysis by mass cytometry and liquid chromatography coupled with tandem mass spectrometry (LC-MS/MS) in addition to single-cell RNA sequencing to reveal the heterogeneous cell populations and extracellular components in malignant ascites. Moreover, we established mesothelial cells derived from malignant ascites and investigated their role in the development of peritoneal dissemination. We divided CD45(−)/EpCAM(−) cells into distinct clusters and identified mesothelial cells with mesenchymal features involved in forming the immunosuppressive microenvironment in malignant ascites. In addition, tenascin-C (TNC) derived from mesothelial cells with mesenchymal features was found to play an essential role in the attachment and colonization of GC cells during peritoneal dissemination processes. Overall, these findings demonstrate the underlying molecular mechanism involved in the shaping of a tumor-promoting microenvironment by nonmalignant cells in ascites.

RESULTS

Proteomic profiling identified defects in immune effectors and the frequent presence of CD45(−)/EpCAM(−) cells in malignant ascites

To evaluate the characteristics of malignant ascites, we performed single-cell mass cytometry powered by CyTOF technology to cluster cell populations using ascites from 30 patients with GC presenting peritoneal dissemination and the ascites of 10 patients with liver cirrhosis (LC) as a control (Figure 1A; Figures S1A and S1B). Although these patients with LC, who need to drain their ascites, often show uncontrollable liver damage and abundant ascites that is not reduced by diuretics and other drugs, we utilized them as those with ascites not associated with cancer (nonmalignant ascites) in the current analyses. As we expected, EpCAM+ cancer cells were the predominant population in malignant ascites; however, various nonmalignant cells were also detected in malignant ascites (Figure 1B). Although the frequency of $CD4^+$ or $CD8^+$ T cells was not different between nonmalignant and malignant ascites, we notably found that $CD163^+$ macrophages among the $CD45^+$ hematopoietic cells were more frequently detected in malignant ascites than in nonmalignant ascites. Additionally, the abundance of cancer cells was positively correlated with the abundance of $CD163^+$ macrophages in malignant ascites (Figure 1C). According to a meta-analysis of 55 studies, a high density of $CD163^+$ tumor-associated macrophages (TAMs) was associated with worse overall survival in patients with various types of cancer, including GC.[7] Moreover, CD163-high TAMs contributed to functional and phenotypic immune subversion of tumor-infiltrating T cells, suggesting an exhausted T cell phenotype, in patients with clear cell renal cell carcinoma (ccRCC).[8] Consistent with the finding in ccRCC tissues, although PD-1 expression was not significant in $CD4^+$ T cells, PD-1 expression in $CD8^+$ T cells was significantly higher in malignant ascites than in nonmalignant ascites (Figure 1D). These findings suggest that the immune surveillance system is attenuated in the malignant ascites of patients with GC with peritoneal dissemination.

Subsequently, we focused on the CD45(−)/EpCAM(−) cell population in ascites. Although this fraction among nonmalignant cells belonged to the mesenchymal cell population, its diversity and significance have not been defined. Intriguingly, the proportion of the CD45(−)/EpCAM(−) cell population was significantly higher in malignant ascites than in nonmalignant ascites (Figure 1E). Additionally, the proportions of cancer cells and CD45(−)/EpCAM(−) cells were positively correlated in malignant ascites (Figure 1F). Although the CD45(−)/EpCAM(−) cell population contained $CD90^-$ and platelet-derived growth factor receptor α (PDGFRα)-rich mesenchymal cells (Figure 1G), we examined the expression of epithelial (EpCAM and cytokeratin), mesothelial (calretinin and ICAM-1), and mesenchymal (CD90 and PDGFRα) markers to further determine the cell lineage.

Figure 1. Attenuated immune surveillance against tumors and the frequent presence of CD45(−)/EpCAM(−) cells in malignant ascites

(A) Experimental workflow for mass cytometric analysis of ascites from patients with gastric cancer (GC) or liver cirrhosis (LC).

(B) t-Distributed stochastic neighbor embedding (t-SNE) visualization of the mass cytometry analysis results for the cell populations in ascites from patients with LC or GC.

(C) Boxplots for the percentage of $CD4^+$ T cells, $CD8^+$ T cells, $CD11b^+/CD163^-$ cells, $CD11b^+/CD163^+$ cells, and other $CD45^+$ cells in the $CD45^+/EpCAM^-$ cell population in ascites from patients with GC or LC. Scatterplots demonstrating Spearman's correlation coefficient r with the percentage of each cell type; cancer cells in malignant ascites are shown on the right side of the boxplots.

(D) Half violin plots showing the expression of PD-1 in $CD4^+$ T cells or $CD8^+$ T cells in ascites from patients with GC or LC.

(E) Percentage of CD45(−)/EpCAM(−) cells in nonmalignant cells in ascites from patients with GC or LC.

(F) Scatterplot demonstrating Spearman's correlation coefficient r of the percentage of CD45(−)/EpCAM(−) and cancer cells in ascites from patients with GC.

(G) t-SNE and histogram visualization of CD90 and PDGFRα expression in the clusters of CD45(−)/EpCAM(−) cells in ascites from patients with GC.

(H) Violin plots showing the comparison of EpCAM, cytokeratin, calretinin, ICAM-1, CD90, and PDGFRα expression between CD45(−)/EpCAM(−) and cancer cells in ascites from patients with GC.

(I) Workflow for single-cell RNA sequencing (scRNA-seq) of ascites from patients with GC with peritoneal metastasis.

(J) scRNA-seq analysis of an unfractionated live-cell mixture from ascites cells. The expression profiles of *EPCAM* and *PTPRC*(−)/*EpCAM*(−) are shown in the UMAP plot.

(K) Expression profiles of *EPCAM*, *KRT8*, *KRT19*, *UPK3B*, *WT1*, *CALB2*, *ICAM1*, *PDGFRA*, and *THY1* are shown in a violin plot with normalized expression levels of the indicated genes.

The results are displayed as the mean ± standard deviation (SD). *$p < 0.05$; ***$p < 0.001$; NS, not significant.

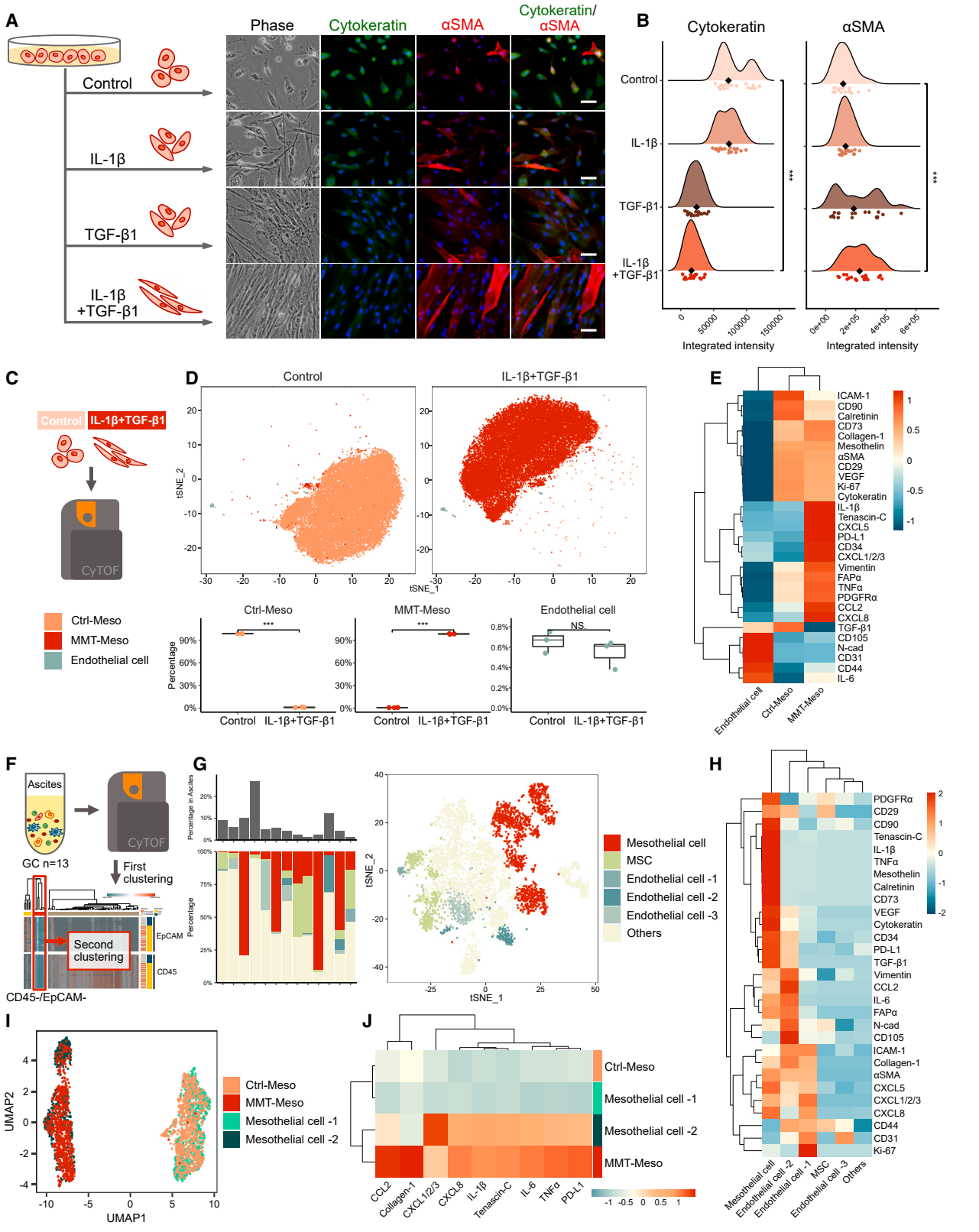

(legend on next page)

Consequently, these cells had abundant mesenchymal and mesothelial markers and maintained cytokeratin expression compared to EpCAM$^+$ cancer cells in malignant ascites of patients with GC (Figure 1H), suggesting that the cell lineage originated from mesothelial cells.

To further characterize the lineage of the CD45(−)/EpCAM(−) cell population, we analyzed single-cell RNA sequencing data of peritoneal metastasis samples from 20 patients with GC as a validation cohort (Figure 1I). We identified CD45(−)/EpCAM(−) cells in the malignant ascites of patients with GC with peritoneal dissemination (Figure 1J). Moreover, CD45(−)/EpCAM(−) cells had abundant mesenchymal (*ICAM1*, *PDGFRA*, and *THY1*) and mesothelial (*UPK3B*, *WT1*, and *CALB2*) markers and maintained cytokeratin (*KRT8* and *KRT19*) expression, as well as mass cytometry results, compared to EpCAM$^+$ cancer cells (Figure 1K). These results strongly support that CD45(−)/EpCAM(−) cells are predominantly derived from mesothelial cells.

Mesothelial cells with mesenchymal features among the CD45(−)/EpCAM(−) cell population exhibit a secretory phenotype in malignant ascites

Mesothelial-mesenchymal transition (MMT)-induced mesothelial cells interact with cancer cells and are considered a subset of cancer-associated fibroblasts in peritoneal metastasis.[9,10] Given that CD45(−)/EpCAM(−) cells express mesenchymal cell markers at high levels, we expected these fractions in malignant ascites to predominantly contain MMT-induced mesothelial cells. Adherent primary mesothelial cells were isolated from the malignant ascites of patients with GC with peritoneal dissemination (Figure S2A). We first examined the markers of mesothelial cells and confirmed the expression of multilineage (epithelial, mesenchymal, and mesothelial) markers (Figure S2B), which are characteristic of mesothelial cells. However, the enriched mesothelial cells showed a cobblestone-like morphology (Figure S2A), suggesting that the MMT phenotype was not maintained during isolation by *in vitro* culture. Therefore, these cells were treated with interleukin-1β (IL-1β), transforming growth factor-β1 (TGF-β1), or IL-1β+TGF-β1, which are known as MMT inducers, to promote the MMT phenotype in mesothelial cells. As we expected, mesothelial cells treated with MMT inducers showed a fibroblastic morphology, a decrease in cytokeratin expression, and an increase in α-smooth muscle actin (αSMA) expression in the immunofluorescence (IF) analysis (Figure 2A). There was a significant difference in cytokeratin and αSMA expression when these cells were treated with IL-1β+TGF-β1 (Figure 2B).

We next performed mass cytometry using mesothelial cells and MMT-induced mesothelial cells to determine the characteristics of these cells and found that the isolated cells contained two different clusters of mesothelial cells and very few CD31$^+$ endothelial cells. Although more than 98% mesothelial cells treated with MMT inducers were translocated into another cluster (MMT-Meso) from the nonstimulated cluster (Ctrl-Meso), endothelial cells were not affected (Figures 2C and 2D). The comparison between Ctrl-Meso and MMT-Meso showed that MMT inducers increased the expression of mesenchymal markers (PDGFRα and vimentin) and decreased the expression of epithelial (cytokeratin) and mesothelial (calretinin and ICAM-1) markers. Moreover, we found that the expression of chemokines (CCL2, CXCL1/2/3 CXCL5, and CXCL8) was significantly higher in the MMT-Meso cluster than in the Ctrl-Meso cluster (Figures 2E; Figure S2C).

Next, to distinguish the mesenchymal cells, we clustered CD45(−)/EpCAM(−) cells in malignant ascites from 13 patients with GC (Figures 2F; Figures S3A–S3C). Although mesothelial cells were the predominant population, we notably determined that endothelial cells expressing CD31 were divided into three clusters and a mesenchymal stem cell (MSC) cluster with CD29, CD44, and CD105 but not CD31 (Figures 2G and 2H). Given the characteristic change in cultured mesothelial cells by MMT induction, we further divided them into two clusters (mesothelial cell 1 and mesothelial cell 2) and compared their similarity with cultured mesothelial cell clusters (Ctrl-Meso and MMT-Meso). Consequently, uniform manifold approximation and projection (UMAP) clustering analysis revealed that mesothelial cell cluster-1 showed similarity to Ctrl-Meso and that mesothelial cell

Figure 2. Secretion phenotype of MMT-induced mesothelial cells in GC ascites

(A) Representative phase-contrast microscopy images or immunofluorescence staining of cytokeratin and αSMA in mesothelial cells stimulated with vehicle control (control), recombinant human IL-1β (IL-1β), recombinant human TGF-β1 (TGF-β1), or a combination of IL-1β and TGF-β1 (IL-1β+TGF-β1). Scale bar: 50 μm.

(B) Fluorescence intensity for cytokeratin and αSMA in each condition in (A).

(C) Experimental workflow: GC ascites-derived mesothelial cells stimulated with vehicle control or the combination of IL-1β and TGF-β1 were analyzed by mass cytometry analysis.

(D) t-SNE plots of control or IL-1β+TGF-β1 cells and the percentages of each cell population in the Ctrl-Meso, MMT-Meso, or endothelial cell clusters are shown in bar plots.

(E) Heatmap showing marker expression of the cells assigned to the Ctrl-Meso, MMT-Meso, or endothelial cell clusters in mass cytometry analysis.

(F) Schematic showing the experimental workflow: ascites from patients with GC (n = 13) were analyzed by mass cytometry, and cells in the CD45(−)/EpCAM(−) population were further clustered.

(G) The percentage of CD45(−)/EpCAM(−) cells in the total cells in each ascites sample is shown on the top left. The proportions of each cell cluster in CD45(−)/EpCAM(−) cells are displayed in stacked bars. The cell populations in CD45(−)/EpCAM(−) cells are depicted by t-SNE visualization.

(H) Heatmap showing unsupervised hierarchical clustering of CD45(−)/EpCAM(−) cells assigned to each cluster in (G) based on the relative protein expression levels in mass cytometry analysis.

(I) UMAP visualization for the integrated dataset of mesothelial cells in (C) and (F). Cells in (C) were annotated based on the clusters in (D), and cells in (F) were further clustered into mesothelial cell 1 and mesothelial cell 2 by their protein expression pattern.

(J) Relative expression levels of selected markers and secreted proteins in the Ctrl-Meso and MMT-Meso clusters from (C) and mesothelial cell 1 and mesothelial cell 2 clusters from (I).

The color in (E), (H), and (J) indicates the *Z* score of protein expression. The results are displayed as the mean ± SD. ***p < 0.001.

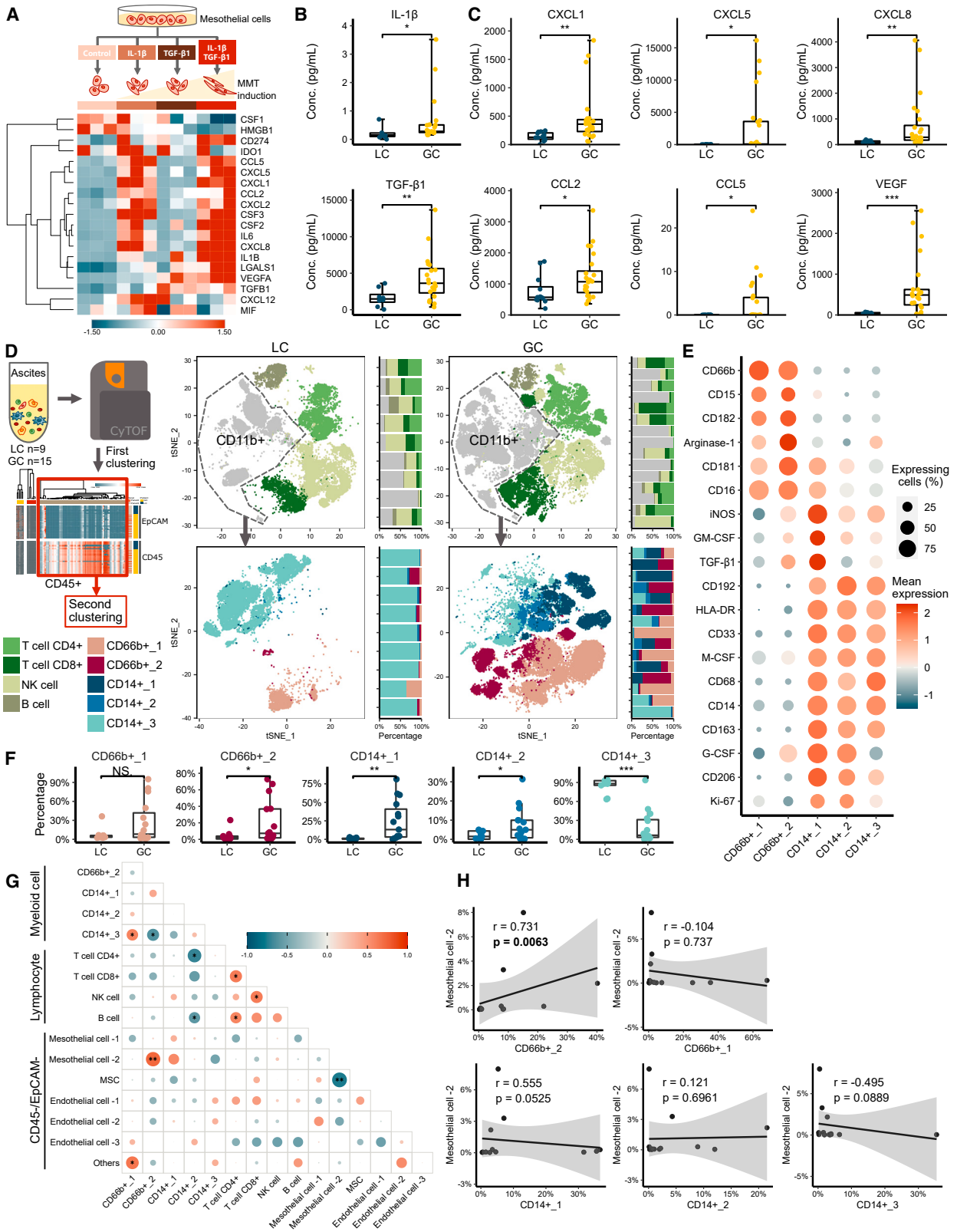

(legend on next page)

cluster-2 completely overlapped with MMT-Meso (Figure 2I). In practice, mesothelial cell cluster-2 in malignant ascites had a similar molecular expression pattern to that of MMT-Meso in *in vitro* culture (Figure 2J). These results imply that mesothelial cell cluster-2 consists of MMT-induced mesothelial cells with mesenchymal features in malignant ascites.

Mesothelial cells with mesenchymal features exhibit a significant correlation with IMCs in malignant ascites

We next performed RNA sequencing using mesothelial cells and MMT-induced mesothelial cells to address the effect of MMT induction on comprehensive gene expression changes. Regarding chemokine expression, IL-1β treatment promoted the expression of chemokines, and the induction was enhanced by additional treatment with TGF-β1 (Figure 3A). We next compared the concentrations of these MMT inducers by ELISA in ascites from patients with GC and LC. The concentrations of both MMT inducers were significantly higher in ascites from patients with GC than in those from patients with LC (Figure 3B). In addition, the protein expression of both MMT inducers was significantly higher in cancer cells than in $CD45^+$ hematopoietic cells in ascites from patients with GC (Figure S3D), suggesting that the predominant source of MMT inducers is cancer cells.

Subsequently, a chemokine bead array revealed that the concentrations of CXCL1, CXCL5, CXCL8, CCL2, CCL5, and vascular endothelial growth factor (VEGF) were significantly higher in ascites from patients with GC than in those from patients with LC (Figure 3C). CXCL1, CXCL5, and CXCL8 are CXCR2 ligands and are closely involved in $CXCR2^+$ polymorphonuclear myeloid-derived suppressor cell (PMN-MDSC) migration into cancer tissues.[11] The CCL2-CCR2 and CCL5-CCR5 axes are known to facilitate the local accumulation of immunosuppressive myeloid cells (IMCs) such as PMN-MDSCs and TAMs.[12,13] Additionally, VEGF family members cause the development of an immunosuppressive tumor microenvironment by inhibiting progenitor cell differentiation to $CD4^+$ and $CD8^+$ lymphocytes while enhancing the effects of immunosuppressive cells such as regulatory T cells (Tregs) and MDSCs.[14,15] Given these previous findings and the current results, there is a possibility that MMT-induced mesothelial cells with mesenchymal features are a source of chemokines involved in the recruitment of immunosuppressive cells, subsequently forming the immunosuppressive microenvironment in malignant ascites.

To investigate the immune cell distribution in malignant ascites, we performed mass cytometry using ascites from 9 patients with LC and 15 patients with GC (Figures 3D; Figures S3A–S3C). $CD45^+$ hematopoietic cells were roughly divided into lymphocytes ($CD4^+$ T cells, $CD8^+$ T cells, natural killer [NK] cells, and B cells) and $CD11b^+$ myeloid cells (Figure S3E). Notably, we found that the frequency of myeloid cells was higher in malignant ascites than in nonmalignant ascites. Therefore, the myeloid cell population was further reclustered into two granulocyte clusters ($CD66b^+$ cluster 1 and 2) and three monocyte clusters ($CD14^+$ cluster 1, 2 and 3), and we found that $CD66b^+$ cluster 2 and $CD14^+$ cluster 1 were predominantly detected in malignant ascites (Figure 3D).

Further comparison among each cluster revealed that $CD66b^+$ cluster 2 exhibited higher expression of arginase-1 and TGF-β1 than $CD66b^+$ cluster 1, indicating that $CD66b^+$ cluster 2 has the characteristics of MDSCs. Among the $CD14^+$ monocyte clusters, $CD14^+$ cluster 1 showed higher expression of iNOS, TGF-β1, CD163, and CD206 than the other two clusters, indicating that TAMs are enriched in $CD14^+$ cluster 1 (Figure 3E). Moreover, the percentages of $CD66b^+$ cluster 2 and $CD14^+$ cluster 1 were significantly higher in malignant ascites from patients with GC than in those from patients with LC (Figure 3F). To investigate whether mesothelial cells with mesenchymal features are involved in immune cell distribution in malignant ascites, correlation plot analysis was performed using mass cytometry data from ascites of 13 patients with GC (Figures 3G; Figure S3C). In particular, we focused on the relationship between mesothelial cell cluster 2, which consists of mesothelial cells with mesenchymal features, and myeloid cell clusters. Notably, we found that the abundance of mesothelial cell cluster 2 was significantly correlated with that of $CD66b^+$ cluster 2, indicating that it consisted of MDSCs (Figures 3G and 3H). These findings suggest that mesothelial cells with mesenchymal features are a source of chemokines and growth factors involved in the accumulation of IMCs in malignant ascites.

TNC derived from MMT-induced mesothelial cells closely interacts with SDC1 on cancer cells

We next carried out a gene set enrichment analysis (GSEA) using RNA sequencing data of mesothelial cells and MMT-induced mesothelial cells, and extracellular matrix (ECM)-related pathways were enriched in MMT-induced mesothelial cells by IL-1β+TGF-β1 treatment (Figure 4A). Specifically, MMT induction promoted the

Figure 3. There was a strong positive correlation between mesothelial cells with mesenchymal features and IMCs in malignant ascites

(A) Heatmap of the relative gene expression levels of soluble factors in the RNA-seq data for mesothelial cells stimulated with each condition.

(B) Quantification of the concentrations of IL-1β and TGF-β1 in ascites from patients with LC or GC by ELISA.

(C) Quantification of the concentrations of CXCL1, CXCL5, CXCL8, CCL2, CCL5, and VEGF in ascites from patients with LC or GC by a chemokine bead array.

(D) Mass cytometry analysis of ascites from patients with LC or GC using an immune cell marker panel. T cell $CD4^+$, T cell $CD8^+$, NK cell, B cell, and $CD11b^+$ clusters in LC or GC ascites are visualized as t-SNE plots, with stacked bar plots showing the percentage of each cluster. The cells in the $CD11b^+$ population were further clustered based on CD66b and CD14 expression and visualized as t-SNE plots, with stacked bar plots displaying the percentage of each cluster in the $CD11b^+$ population.

(E) Expression levels of selected markers and secreted proteins in clusters in the $CD11b^+$ population. The sizes of circles indicate the percentages of expressing cells in each cluster, and the color indicates the mean protein expression level.

(F) Quantification of the proportion of each cell cluster in the $CD11b^+$ population in ascites from patients with LC or GC.

(G) Correlation coefficient matrix summarizing associations between the proportions of each cell cluster in GC ascites. The sizes of the circles indicate the absolute values of the corresponding correlation coefficients.

(H) Scatterplots demonstrating Spearman's correlation coefficient r of the percentage of the mesothelial cell 2 cluster and $CD66^+$ or $CD14^+$ cluster in GC ascites. The results are displayed as the mean ± SD. *$p < 0.05$; **$p < 0.01$; ***$p < 0.001$; NS, not significant.

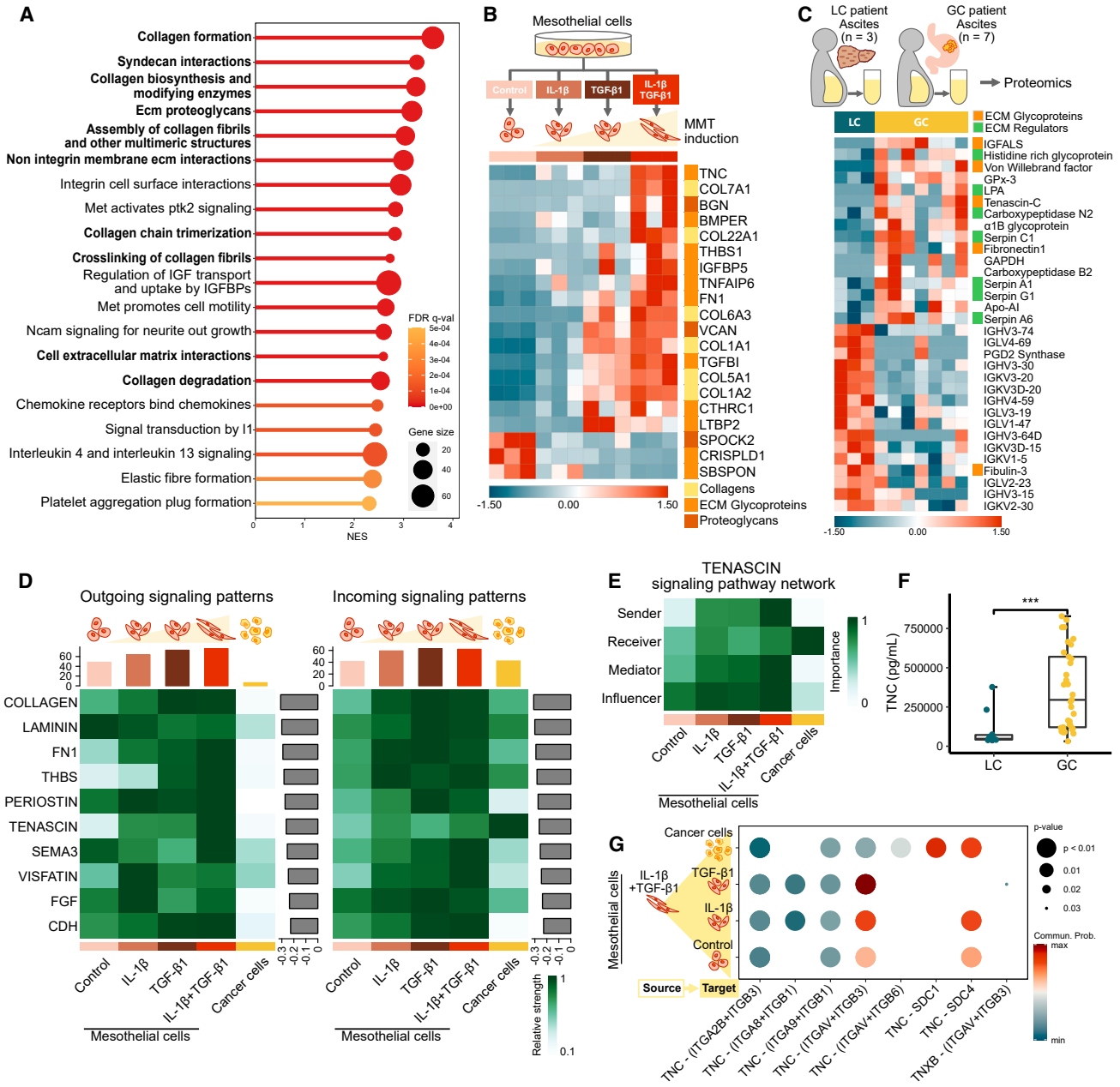

Figure 4. Close interaction between TNC from MMT-induced mesothelial cells and SDC1 on cancer cells

(A) Enriched Gene Ontology (GO) terms in GSEA for the RNA-seq data of mesothelial cells stimulated with IL-1β and TGF-β1. The sizes of the circles indicate the enrichment of genes in each GO term, and the color indicates the false discovery rate (FDR) q values.

(B) Heatmap of the relative expression levels of extracellular-matrix-related genes in the RNA-seq data for mesothelial cells stimulated with each condition.

(C) Proteomic analysis of ascites from patients with LC (n = 3) and GC (n = 7) by mass spectrometry; the results are summarized as a heatmap with unsupervised hierarchical clustering.

(D) CellChat analysis of the RNA-seq data for mesothelial cells stimulated with each condition together with previously reported RNA-seq data of cancer cells in GC ascites. Heatmap showing the predicted contribution of the top 10 signals in cell-cell communication among the cell groups.

(E) Relative contribution of each cell as a sender, receiver, mediator, or influencer in the TENASCIN signaling pathway among the interactions of mesothelial cells and cancer cells in GC ascites.

(F) Quantification of the concentrations of TNC in ascites from patients with LC or GC by ELISA. The results are displayed as the mean ± SD. ***$p < 0.001$.

(G) Bubble plot showing a significant ligand-receptor interaction pairs of the TENASCIN signaling pathway between mesothelial cells stimulated with IL-1β + TGF-β1 and other cells. The sizes of the circles indicate p values, and the color indicates communication probability.

gene expression of ECM proteins, such as collagens, fibronectin, and TNC, among differentially expressed genes (DEGs) in mesothelial cells (Figure 4B). Given the RNA sequencing data, we conducted a comprehensive proteomic analysis using ascites from 3 patients with LC and 7 patients with GC. Although immunoglobulins were predominantly detected in the ascites of patients with LC, ECM glycoproteins and regulators such as fibronectin, TNC, and serpin family members were enriched as extracellular components in the malignant ascites of patients with GC (Figure 4C).

To address the intercellular signaling crosstalk between MMT-induced mesothelial cells and cancer cells, we performed CellChat analysis using RNA sequencing data of MMT-induced mesothelial cells and an RNA sequencing dataset of $EpCAM^+$ GC cells from ascites.[3] CellChat analysis enables the identification of specific signaling roles in intercellular communications in individual cell populations.[16] Most ECM signals were recognized as outgoing signals by MMT-induced mesothelial cells, whereas we identified TENASCIN as an incoming signal in cancer cells, indicating a specific signal receiver (Figures 4D and 4E). In practice, we confirmed that TNC levels were significantly higher in the ascites of 30 patients with GC presenting peritoneal dissemination than in those of the 10 patients with LC (Figure 4F), suggesting that cancer cells are likely to receive stimulation by TNC in malignant ascites.

To further investigate the TNC isoform, we performed long-read direct RNA sequencing in mesothelial cells treated with IL-1β+TGF-β1. Consequently, we found that TNC isoform 3 was predominantly expressed in mesothelial cells treated with IL-1β+TGF-β1 (Figure S4). Given that alternatively spliced domains contain binding sites for receptor proteins,[17] we examined the ligand-receptor interaction pair of the TENASCIN signaling pathway. Consequently, among all known ligand-receptor pairs, the interaction between TNC in MMT-induced mesothelial cells and syndecan-1 (SDC1) in cancer cells showed a prominent contribution (Figure 4G). These findings suggest that the interaction between TNC derived from MMT-induced mesothelial cells with mesenchymal features and SDC1 on cancer cells plays an important role in peritoneal dissemination.

TNC derived from MMT-induced mesothelial cells enhances the attachment and growth of floating cancer cells

To investigate the importance of TNC from MMT-induced mesothelial cells in peritoneal dissemination, we first conducted sphere formation assays using normal medium, ascites from patients with GC, conditioned medium (CM) from mesothelial cells (control-CM) or CM from MMT-induced mesothelial cells (MMT-CM) under nonattachment conditions. However, the GC spheroid sizes were not different among the groups (Figure 5A; Figure S5A). These results suggest that mesothelial-cell-derived factors do not influence the sphere-formation ability of GC cells.

Therefore, we next performed a spheroid attachment assay. This assay model demonstrates that tumor spheroid attachment and spreading on a mesothelial monolayer promote clearance of mesothelial cells from the area underneath the spheroid.[18] Notably, we found that the GC spheroid spreading area was significantly larger in the MMT-induced mesothelial cell group than in the mesothelial cell group (Figure 5B; Video S1). IF analysis revealed that TNC accumulated around the spread GC cells (Figure 5C). We then conducted a loss-of-function study using two independent small interfering RNAs (siRNAs) for TNC to show the importance of TNC in the attachment and growth of GC spheroids. Strikingly, TNC depletion in MMT-induced mesothelial cells diminished GC spheroid attachment and spreading on a mesothelial monolayer (Figure 5D). This finding suggests that TNC plays an essential role in the attachment and colonization of GC cells.

Given these findings, we examined the existence and source of TNC in peritoneal disseminated tumors from patients with GC. We first found cytokeratin/αSMA/calretinin triple-positive mesothelial cells around cytokeratin/EpCAM/SDC1 triple-positive GC cells in peritoneal tumors. TNC was specifically expressed in mesothelial cells, supporting the observation that TNC expression was induced by MMT induction in cultured mesothelial cells (Figures 5E; Figure S5B). These findings from *in vitro* assays and human peritoneal dissemination suggest that TNC derived from MMT-induced mesothelial cells with mesenchymal features enhances the attachment and growth of GC cells to create a form of peritoneal dissemination.

TNC plays an essential role in peritoneal dissemination

To further investigate the role of TNC in peritoneal dissemination *in vivo*, we conducted peritoneal dissemination model experiments using a mouse GC cell line (GAN-KP cells) established from K19-Wnt1/C2mE transgenic (GAN) mice.[19–21] Given the previous findings that loss of function of the *Cdh1* gene, encoding E-cadherin, is associated with hereditary diffuse GC (HDGC) in humans and tumors with a diffuse morphology similar to signet-ring cell carcinoma in mice,[22,23] we established *Cdh1* knockout GAN-KP cells (GAN-KPC cells). We first confirmed that E-cadherin protein expression at the membrane was lost, along with maintenance of SDC1 expression in GAN-KPC cells (Figure 6A; Figure S6A). Morphological examination revealed that attachment to culture dishes and cell-cell contact were weakened in GAN-KPC cells (Figure 6A). Then, we injected GAN-KP or GAN-KPC cells into the peritoneal cavity of wild-type mice and investigated the peritoneal tumor-formation ability (Figure 6B). Body weight loss was apparent 18 days after inoculation with GAN-KPC cells (Figure S6B). Moreover, the peritoneal tumors formed by GAN-KPC cells 21 days after inoculation were significantly larger than the tumors formed by GAN-KP cells (Figure 6C). Along with peritoneal tumor formation, GAN-KPC-inoculated mice had a much larger amount of ascites than GAN-KP-inoculated mice (Figure 6C). Given that we successfully developed a peritoneal dissemination model using GAN-KPC cells, we next utilized *Tnc* knockout (*Tnc*-KO) mice to investigate the importance of TNC in peritoneal dissemination (Figure 6D). Consequently, the peritoneal tumors formed by GAN-KPC cells in *Tnc*-KO mice were significantly smaller than the tumors formed by these cells in wild-type mice (Figure 6E). Body weight loss and ascites accumulation were suppressed in GAN-KPC-inoculated *Tnc*-KO mice (Figures 6E and 6F). These results, together with the findings of the spheroid attachment assay, suggest that TNC plays an important role in the attachment and growth of GC cells during peritoneal tumor formation.

To further address the significance of the interaction between TNC and SDC1 in peritoneal tumor formation, we established

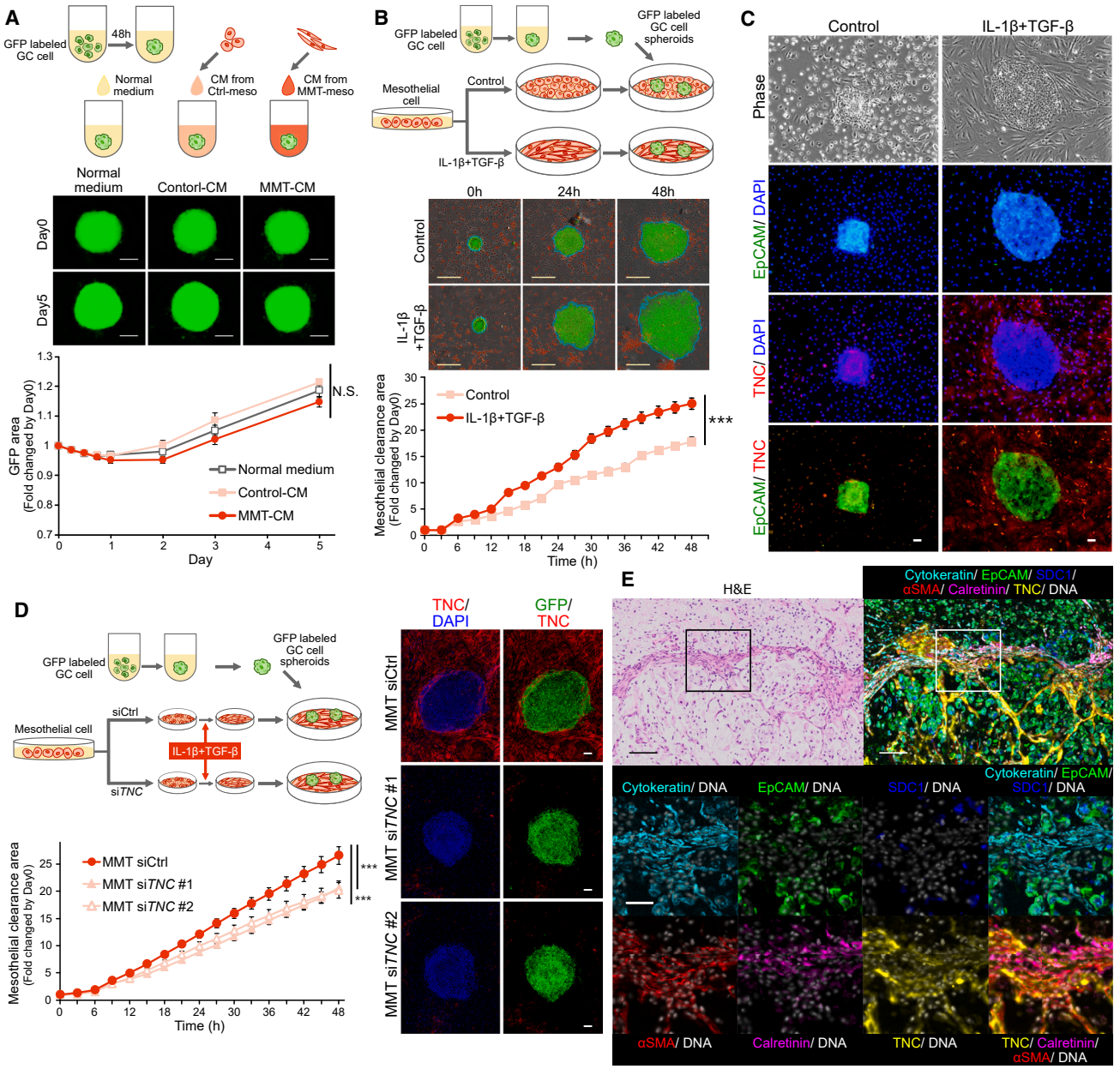

Figure 5. Enhanced colonization and growth of cancer cells by TNC from MMT-induced mesothelial cells

(A) Schematic showing the experimental workflow of the sphere-formation assay and representative fluorescence microscopy images of colonies in each condition on days 0 and 5. The growth of colonies in each condition was quantified as the GFP area of colonies normalized to day 0 and is shown on the bottom. Scale bar: 100 μm.

(B) Schematic showing the experimental workflow of the spheroid attachment assay and representative images of fluorescence microscopy of colonies in the control or IL-1β+TGF-β1 group at 0, 24, and 48 h. The mesothelial cell cleared area in each group was detected by IncuCyte S3 and is quantified on the bottom. Scale bar: 400 μm.

(C) Immunofluorescence staining of EpCAM and TNC for colonies in the control or IL-1β+TGF-β1 group. Scale bar: 100 μm.

(D) GC spheroid attachment assay with *TNC*-depleted mesothelial cells (si*TNC* #1 and #2). Representative immunofluorescence staining images for the colonies in each condition are shown on the right. The mesothelial cell cleared area in each condition was quantified and is displayed on the bottom.

(E) Representative images of hematoxylin-eosin (H&E) staining and fluorescent immunohistochemical staining of cytokeratin, EpCAM, SDC1, αSMA, calretinin, and TNC in peritoneal disseminated tissue from a patient with GC. Scale bars: 100 μm and 50 μm (magnified images).

The results are displayed as the mean ± SD. ***p < 0.001; NS, not significant.

CellPress
OPEN ACCESS

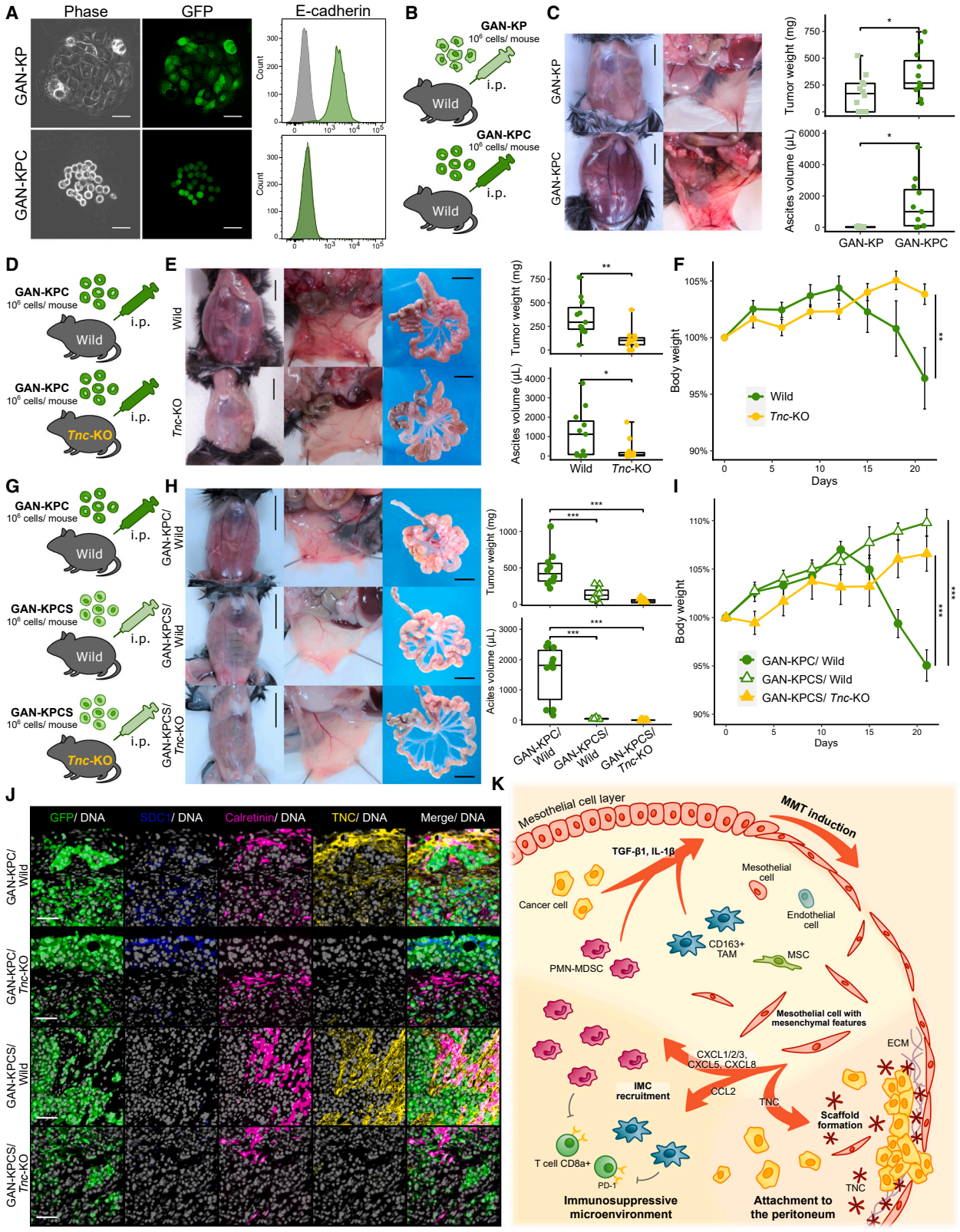

(legend on next page)

Sdc1-KO GAN-KPC cells, named GAN-KPCS cells, and compared peritoneal tumor formation using GAN-KPC and GAN-KPCS cells (Figures 6G; Figure S6A). Consequently, Sdc1 KO significantly reduced tumor weight and ascites accumulation and recovered body weight loss. Moreover, the tumors were almost diminished, and body weight loss was not detected when GAN-KPCS cells were inoculated into the peritoneal cavity of *Tnc*-KO mice (Figures 6H and 6I). We finally confirmed that peritoneal tumors formed in *Tnc*-KO mice did not contain TNC and that peritoneal tumors formed by GAN-KPCS cells did not express SDC1 (Figure 6J). These results suggest that the interaction between TNC and SDC1 plays a critical role in peritoneal tumor formation.

DISCUSSION

Peritoneal dissemination occurs in patients with advanced gastrointestinal cancers and ovarian cancers and is frequently accompanied by the accumulation of ascites. The peritoneal cavity is covered by a monolayer of mesothelial cells, and MMT induction in mesothelial cells enhances peritoneal fibrogenesis in patients receiving peritoneal dialysis[24] and dissemination in patients with ovarian cancer.[9,10] In the peritoneal fluid of patients with advanced cancer, $CD90^{+}/CD45^{-}$ cells have been identified as a minor but distinct population.[25] These cells, called mesothelial-like cells, share the characteristics of MSCs and significantly enhanced metastasis in the peritoneum of a xenograft model.[26] In our previous study, we demonstrated that $CD90^{+}/PDGFR\alpha^{+}$ mesenchymal cells exhibit senescent and secretory phenotypes.[27] However, the diversity of mesenchymal cells in malignant ascites has not been determined. In the current study, single-cell proteomic profiling of malignant ascites revealed that the CD45(−)/EpCAM(−) cell population was divided into distinct populations based on the cell of origin: endothelial cells, mesothelial cells, and MSCs. We also demonstrated that MMT-induced mesothelial cells with mesenchymal features are a predominant source of chemokines that recruit IMCs and ECM proteins, especially TNC, involved in cancer cell colonization in the peritoneum.

TNC is an ECM glycoprotein, and its physiological expression is limited in connective tissues and stem cell niches of several adult tissues, suggesting a role in stem cell regulation.[28] However, TNC production is strongly induced under pathological conditions such as inflammation and in the cancer stroma. TNC expression at invasive fronts of cancer tissues promotes cancer cell invasion and is linked to poor clinical outcome.[29,30] The TNC protein consists of several structural domains that play distinct roles in its function, and various integrins can bind to the tripeptide sequence Arg-Gly-Asp in the fibronectin type III-like domain of TNC and enhance EMT-like changes in cancer cells.[17] Although SDC4 can also interact with TNC and enhance cancer cell growth,[31] the significance and corresponding receptor of TNC in peritoneal dissemination have not been determined. We identified a close interaction between TNC from MMT-induced mesothelial cells and SDC1 on GC cells by CellChat analysis in this study. Based on the marked reduction in peritoneal tumor formation caused by KPC and KPCS cells in *Tnc*-KO mice, the TNC/SDC1 interaction may play an essential role in peritoneal dissemination. Although SDC1 has been reported to be a receptor for ECM components, such as collagen and fibronectin, and acts as a mediator of cancer cell growth and invasion by regulating integrin activity,[32,33] we demonstrated for the first time the importance of the TNC/SDC1 interaction in peritoneal dissemination. Given that treatment strategies targeting SDC1 are being clinically investigated in the context of various types of cancer,[34] the current findings regarding the TNC/SDC1 interaction may provide a rational therapeutic target for patients with cancer with peritoneal dissemination.

Evidence that mesenchymal cells orchestrate the functions of immune cells and cause immunosuppression in cancer tissues has been collected.[5,35] CXCL12 from fibroblast activation protein $(FAP)^{+}$ cancer-associated fibroblasts (CAFs) suppresses T cell recruitment into the tumor microenvironment and causes the formation of a local immunosuppressive environment.[36] Activated stellate cells block the infiltration of $CD8^{+}$ T cells in the compartments adjacent to tumor cells in human and mouse pancreatic ductal adenocarcinomas.[37] Although these phenomena have been investigated in primary tumors, the immune microenvironment in the peritoneal cavity during the development of peritoneal dissemination is completely unknown. In the

Figure 6. Essential role of TNC from mesothelial cells with mesenchymal features in CG cell peritoneal dissemination

(A) Representative images of phase-contrast and fluorescence microscopy of GAN-KP or GAN-KPC cells with a histogram of the mean fluorescence intensity of E-cadherin. Scale bar: 50 μm.

(B) Schematic of the experimental design: GAN-KP or GAN-KPC cells were intraperitoneally injected into wild-type C57BL/6 mice (n = 11).

(C) The gross appearance of the abdominal wall and cavity of mice injected with GAN-KP or GAN-KPC cells. Quantification of the weight of tumors and the volume of ascites from each group on day 21 is shown on the right. Scale bar: 10 mm.

(D) Schematic of the experimental design: GAN-KPC cells were intraperitoneally injected into wild-type or *Tnc* knockout (*Tnc*-KO) C57BL/6 mice (n = 11).

(E) The gross appearance of the abdominal wall and cavity as well as the mesenterium of wild-type or *Tnc*-KO mice is shown on the left. Scale bar: 10 mm. Quantification of the weight of tumors and the volume of ascites from each group on day 21 is shown on the right. Scale bar: 10 mm.

(F) Body weight curves of wild-type or *Tnc*-KO mice injected with GAN-KPC cells.

(G) Schematic of the experimental design: GAN-KPC cells were intraperitoneally injected into wild-type C57BL/6 mice, and GAN-KPCS cells were intraperitoneally injected into wild-type or *Tnc*-KO C57BL/6 mice (n = 10, respectively).

(H) The gross appearance of the abdominal wall and cavity as well as the mesenterium of the mouse from each group. Scale bar: 10 mm. Quantification of the weight of tumors and the volume of ascites from each group on day 21 is shown on the right. Scale bar: 10 mm.

(I) Body weight curves of the mice from each group.

(J) Representative images of fluorescent immunohistochemical staining of GFP, SDC1, calretinin, and TNC in peritoneal disseminating tumors from the indicated groups. Scale bar: 50 μm.

(K) Schematic of the proposed mechanism for the development of an immunosuppressive and protumorigenic microenvironment in the peritoneal cavity by mesothelial cells with mesenchymal features.

The results are displayed as the mean ± SD. *p < 0.05; **p < 0.01; ***p < 0.001.

current study, cell population analysis by mass cytometry revealed that IMCs, such as CD163$^+$ TAMs and PMN-MDSCs, were enriched in malignant ascites. In addition, the abundance of IMCs was significantly correlated with that of mesothelial cell cluster 2, exhibiting abundant chemokines involved in MDSC recruitment, according to the correlation plot analysis. Together with our observation that mesothelial cell cluster 2 in malignant ascites had a similar gene expression pattern to MMT-Meso in *in vitro* culture, the results suggest that MMT-induced mesothelial cells with mesenchymal features are responsible for the immunosuppressive microenvironment in the malignant ascites of patients with GC with peritoneal dissemination. A comprehensive understanding of the crosstalk among cancer cells, mesenchymal cells, and immune cells in the peritoneal cavity may confer a novel ability to control peritoneal dissemination.

In summary, IL-1β and TGF-β1, as MMT inducers, are concentrated in the malignant ascites of patients with GC and promote the MMT phenotype of mesothelial cells. CD45(−)/EpCAM(−) cells in malignant ascites include mesothelial cells with mesenchymal features, endothelial cells, and MSCs. Mesothelial cells with mesenchymal features facilitate IMC recruitment through specific chemokines and attachment to the peritoneum through TNC production as a scaffold for GC cells, leading to enhanced peritoneal dissemination (Figure 6K). The findings in the current study reveal the existence of a tumor-promoting microenvironment by single-cell proteomic profiling and the distinct roles of the mesenchymal cell population in malignant ascites. Therefore, a combined treatment strategy targeting the protumorigenic microenvironment with cancer cells should be developed to completely cure patients with cancer with peritoneal dissemination.

Limitations of the study

The current study contains several limitations. First, we utilized the ascites of patients with LC as a control (nonmalignant ascites) in the current analyses. However, patients with LC show abundant ascites along with uncontrollable liver damage, and the ascites from patients with LC are not an actually healthy controls. Second, we demonstrated that CD45(−)/EpCAM(−) cells in malignant ascites include mesothelial cells with mesenchymal features, endothelial cells and MSCs. However, CD45(−)/EpCAM(−) cells still contain unclustered cells. This result was due to the technical limitations of mass cytometry. Third, although we revealed the existence of an immunosuppressive microenvironment in malignant ascites, the significance of immunosuppression in peritoneal dissemination should be further investigated in mouse models.

STAR★METHODS

Detailed methods are provided in the online version of this paper and include the following:

SUPPLEMENTAL INFORMATION

Supplemental information can be found online at https://doi.org/10.1016/j.celrep.2023.113613.

ACKNOWLEDGMENTS

We thank S. Usuki and N. Tani (Liaison Laboratory Research Promotion Center, IMEG, Kumamoto University) for assisting with RNA sequencing and proteomics. This work was supported by the FOREST program of the Japan Science and Technology Agency (JST, grant no. JPMJFR200H to T.I.); AMED (grant no. 23ama221421 to T.I.); the Japan Society for the Promotion of Science (JSPS, KAKENHI grant nos. 220K09038, 21KK0153, and 23H02772 to T.I., 23H02998 to T.S., 23K08051 to T.Y., and 23K08113 to T.U.); the Naito Foundation; the Suzuken Memorial Foundation; the Chugai Foundation for Innovative Drug Discovery Science; and the Shinnihon Foundation of Advanced Medical Treatment Research.

AUTHOR CONTRIBUTIONS

Conception and design, A.Y. and T.I.; data acquisition, A.Y., Y.F., H.W., and N.Y.-Y.; data analysis and interpretation (e.g., RNA sequencing, computational analysis), T.S., J.Z., Y.F., N.Y.-Y, T.U., T.Y., and T.I.; manuscript writing, review, and/or revision, A.Y., T.S., Y.F., and T.I.; administrative, technical, or material support, A.N., L.F., X.H., F.W., F.K., T.A., K.Y., K.E., S.I., M.I., Y.M., K.M., J.Y., O.N., and H.S.; study supervision, S.S., P.T., H.B., J.A.A., and T.I.

DECLARATION OF INTERESTS

The authors declare no competing interests.

Received: February 3, 2023
Revised: September 13, 2023
Accepted: December 7, 2023
Published: January 16, 2024

REFERENCES

1. Wang, R., Dang, M., Harada, K., Han, G., Wang, F., Pool Pizzi, M., Zhao, M., Tatlonghari, G., Zhang, S., Hao, D., et al. (2021). Single-cell dissection of intratumoral heterogeneity and lineage diversity in metastatic gastric adenocarcinoma. Nat. Med. *27*, 141–151.
2. Kim, S.T., Cristescu, R., Bass, A.J., Kim, K.M., Odegaard, J.I., Kim, K., Liu, X.Q., Sher, X., Jung, H., Lee, M., et al. (2018). Comprehensive molecular characterization of clinical responses to PD-1 inhibition in metastatic gastric cancer. Nat. Med. *24*, 1449–1458.
3. Tanaka, Y., Chiwaki, F., Kojima, S., Kawazu, M., Komatsu, M., Ueno, T., Inoue, S., Sekine, S., Matsusaki, K., Matsushita, H., et al. (2021). Multi-omic profiling of peritoneal metastases in gastric cancer identifies molecular subtypes and therapeutic vulnerabilities. Nat. Can. (Ott.) *2*, 962–977.
4. Navas, T., Kinders, R.J., Lawrence, S.M., Ferry-Galow, K.V., Borgel, S., Hollingshead, M.G., Srivastava, A.K., Alcoser, S.Y., Makhlouf, H.R., Chuaqui, R., et al. (2020). Clinical Evolution of Epithelial-Mesenchymal Transition in Human Carcinomas. Cancer Res. *80*, 304–318.
5. Bu, L., Baba, H., Yoshida, N., Miyake, K., Yasuda, T., Uchihara, T., Tan, P., and Ishimoto, T. (2019). Biological heterogeneity and versatility of cancer-associated fibroblasts in the tumor microenvironment. Oncogene *38*, 4887–4901.
6. Vegliante, R., Pastushenko, I., and Blanpain, C. (2022). Deciphering functional tumor states at single-cell resolution. EMBO J. *41*, e109221.
7. Zhang, Q.W., Liu, L., Gong, C.Y., Shi, H.S., Zeng, Y.H., Wang, X.Z., Zhao, Y.W., and Wei, Y.Q. (2012). Prognostic significance of tumor-associated macrophages in solid tumor: a meta-analysis of the literature. PLoS One *7*, e50946.
8. Dannenmann, S.R., Thielicke, J., Stöckli, M., Matter, C., von Boehmer, L., Cecconi, V., Hermanns, T., Hefermehl, L., Schraml, P., Moch, H., et al. (2013). Tumor-associated macrophages subvert T-cell function and correlate with reduced survival in clear cell renal cell carcinoma. OncoImmunology *2*, e23562.
9. Sandoval, P., Jiménez-Heffernan, J.A., Rynne-Vidal, Á., Pérez-Lozano, M.L., Gilsanz, Á., Ruiz-Carpio, V., Reyes, R., García-Bordas, J., Stamatakis, K., Dotor, J., et al. (2013). Carcinoma-associated fibroblasts derive from mesothelial cells via mesothelial-to-mesenchymal transition in peritoneal metastasis. J. Pathol. *231*, 517–531.
10. Rynne-Vidal, A., Au-Yeung, C.L., Jiménez-Heffernan, J.A., Pérez-Lozano, M.L., Cremades-Jimeno, L., Bárcena, C., Cristóbal-García, I., Fernández-Chacón, C., Yeung, T.L., Mok, S.C., et al. (2017). Mesothelial-to-mesenchymal transition as a possible therapeutic target in peritoneal metastasis of ovarian cancer. J. Pathol. *242*, 140–151.
11. Cheng, Y., Ma, X.L., Wei, Y.Q., and Wei, X.W. (2019). Potential roles and targeted therapy of the CXCLs/CXCR2 axis in cancer and inflammatory diseases. Biochim. Biophys. Acta Rev. Canc *1871*, 289–312.
12. Li, F., Kitajima, S., Kohno, S., Yoshida, A., Tange, S., Sasaki, S., Okada, N., Nishimoto, Y., Muranaka, H., Nagatani, N., et al. (2019). Retinoblastoma Inactivation Induces a Protumoral Microenvironment via Enhanced CCL2 Secretion. Cancer Res. *79*, 3903–3915.
13. Ban, Y., Mai, J., Li, X., Mitchell-Flack, M., Zhang, T., Zhang, L., Chouchane, L., Ferrari, M., Shen, H., and Ma, X. (2017). Targeting Autocrine CCL5-CCR5 Axis Reprograms Immunosuppressive Myeloid Cells and Reinvigorates Antitumor Immunity. Cancer Res. *77*, 2857–2868.
14. Ohm, J.E., Gabrilovich, D.I., Sempowski, G.D., Kisseleva, E., Parman, K.S., Nadaf, S., and Carbone, D.P. (2003). VEGF inhibits T-cell development and may contribute to tumor-induced immune suppression. Blood *101*, 4878–4886.
15. Rahma, O.E., and Hodi, F.S. (2019). The Intersection between Tumor Angiogenesis and Immune Suppression. Clin. Cancer Res. *25*, 5449–5457.
16. Jin, S., Guerrero-Juarez, C.F., Zhang, L., Chang, I., Ramos, R., Kuan, C.H., Myung, P., Plikus, M.V., and Nie, Q. (2021). Inference and analysis of cell-cell communication using CellChat. Nat. Commun. *12*, 1088.
17. Yoshida, T., Akatsuka, T., and Imanaka-Yoshida, K. (2015). Tenascin-C and integrins in cancer. Cell Adhes. Migrat. *9*, 96–104.
18. Iwanicki, M.P., Davidowitz, R.A., Ng, M.R., Besser, A., Muranen, T., Merritt, M., Danuser, G., Ince, T.A., and Brugge, J.S. (2011). Ovarian cancer spheroids use myosin-generated force to clear the mesothelium. Cancer Discov. *1*, 144–157.
19. Oshima, H., Matsunaga, A., Fujimura, T., Tsukamoto, T., Taketo, M.M., and Oshima, M. (2006). Carcinogenesis in mouse stomach by simultaneous activation of the Wnt signaling and prostaglandin E2 pathway. Gastroenterology *131*, 1086–1095.
20. Okazaki, S., Shintani, S., Hirata, Y., Suina, K., Semba, T., Yamasaki, J., Umene, K., Ishikawa, M., Saya, H., and Nagano, O. (2018). Synthetic lethality of the ALDH3A1 inhibitor dyclonine and xCT inhibitors in glutathione deficiency-resistant cancer cells. Oncotarget *9*, 33832–33843.
21. Yamasaki, J., Hirata, Y., Otsuki, Y., Suina, K., Saito, Y., Masuda, K., Okazaki, S., Ishimoto, T., Saya, H., and Nagano, O. (2022). MEK inhibition suppresses metastatic progression of KRAS-mutated gastric cancer. Cancer Sci. *113*, 916–925.
22. Humar, B., Blair, V., Charlton, A., More, H., Martin, I., and Guilford, P. (2009). E-cadherin deficiency initiates gastric signet-ring cell carcinoma in mice and man. Cancer Res. *69*, 2050–2056.
23. Seidlitz, T., Chen, Y.T., Uhlemann, H., Schölch, S., Kochall, S., Merker, S.R., Klimova, A., Hennig, A., Schweitzer, C., Pape, K., et al. (2019). Mouse Models of Human Gastric Cancer Subtypes With Stomach-Specific CreERT2-Mediated Pathway Alterations. Gastroenterology *157*, 1599–1614.e2.
24. Si, M., Wang, Q., Li, Y., Lin, H., Luo, D., Zhao, W., Dou, X., Liu, J., Zhang, H., Huang, Y., et al. (2019). Inhibition of hyperglycolysis in mesothelial cells prevents peritoneal fibrosis. Sci. Transl. Med. *11*, eaav5341.
25. Ho, C.M., Chang, S.F., Hsiao, C.C., Chien, T.Y., and Shih, D.T.B. (2012). Isolation and characterization of stromal progenitor cells from ascites of patients with epithelial ovarian adenocarcinoma. J. Biomed. Sci. *19*, 23.
26. Kitayama, J., Emoto, S., Yamaguchi, H., Ishigami, H., and Watanabe, T. (2014). CD90+ mesothelial-like cells in peritoneal fluid promote peritoneal metastasis by forming a tumor permissive microenvironment. PLoS One *9*, e86516.
27. Yasuda, T., Koiwa, M., Yonemura, A., Miyake, K., Kariya, R., Kubota, S., Yokomizo-Nakano, T., Yasuda-Yoshihara, N., Uchihara, T., Itoyama, R., et al. (2021). Inflammation-driven senescence-associated secretory phenotype in cancer-associated fibroblasts enhances peritoneal dissemination. Cell Rep. *34*, 108779.
28. Chiquet-Ehrismann, R., Orend, G., Chiquet, M., Tucker, R.P., and Midwood, K.S. (2014). Tenascins in stem cell niches. Matrix Biol. *37*, 112–123.
29. Jahkola, T., Toivonen, T., von Smitten, K., Blomqvist, C., and Virtanen, I. (1996). Expression of tenascin in invasion border of early breast cancer correlates with higher risk of distant metastasis. Int. J. Cancer *69*, 445–447.
30. Lowy, C.M., and Oskarsson, T. (2015). Tenascin C in metastasis: A view from the invasive front. Cell Adhes. Migrat. *9*, 112–124.
31. Huang, W., Chiquet-Ehrismann, R., Moyano, J.V., Garcia-Pardo, A., and Orend, G. (2001). Interference of tenascin-C with syndecan-4 binding to fibronectin blocks cell adhesion and stimulates tumor cell proliferation. Cancer Res. *61*, 8586–8594.
32. Rapraeger, A.C., Ell, B.J., Roy, M., Li, X., Morrison, O.R., Thomas, G.M., and Beauvais, D.M. (2013). Vascular endothelial-cadherin stimulates syndecan-1-coupled insulin-like growth factor-1 receptor and cross-talk between alphaVbeta3 integrin and vascular endothelial growth factor receptor 2 at the onset of endothelial cell dissemination during angiogenesis. FEBS J. *280*, 2194–2206.

33. Stepp, M.A., Pal-Ghosh, S., Tadvalkar, G., and Pajoohesh-Ganji, A. (2015). Syndecan-1 and Its Expanding List of Contacts. Adv. Wound Care *4*, 235–249.

34. Yang, Z., Chen, S., Ying, H., and Yao, W. (2022). Targeting syndecan-1: new opportunities in cancer therapy. Am. J. Physiol. Cell Physiol. *323*, C29–C45.

35. Bu, L., Baba, H., Yasuda, T., Uchihara, T., and Ishimoto, T. (2020). Functional diversity of cancer-associated fibroblasts in modulating drug resistance. Cancer Sci. *111*, 3468–3477.

36. Feig, C., Jones, J.O., Kraman, M., Wells, R.J.B., Deonarine, A., Chan, D.S., Connell, C.M., Roberts, E.W., Zhao, Q., Caballero, O.L., et al. (2013). Targeting CXCL12 from FAP-expressing carcinoma-associated fibroblasts synergizes with anti-PD-L1 immunotherapy in pancreatic cancer. Proc. Natl. Acad. Sci. USA *110*, 20212–20217.

37. Ene-Obong, A., Clear, A.J., Watt, J., Wang, J., Fatah, R., Riches, J.C., Marshall, J.F., Chin-Aleong, J., Chelala, C., Gribben, J.G., et al. (2013). Activated pancreatic stellate cells sequester CD8+ T cells to reduce their infiltration of the juxtatumoral compartment of pancreatic ductal adenocarcinoma. Gastroenterology *145*, 1121–1132.

38. Dobin, A., Davis, C.A., Schlesinger, F., Drenkow, J., Zaleski, C., Jha, S., Batut, P., Chaisson, M., and Gingeras, T.R. (2013). STAR: ultrafast universal RNA-seq aligner. Bioinformatics *29*, 15–21.

39. Subramanian, A., Tamayo, P., Mootha, V.K., Mukherjee, S., Ebert, B.L., Gillette, M.A., Paulovich, A., Pomeroy, S.L., Golub, T.R., Lander, E.S., and Mesirov, J.P. (2005). Gene set enrichment analysis: a knowledge-based approach for interpreting genome-wide expression profiles. Proc. Natl. Acad. Sci. USA *102*, 15545–15550.

40. Mootha, V.K., Lindgren, C.M., Eriksson, K.F., Subramanian, A., Sihag, S., Lehar, J., Puigserver, P., Carlsson, E., Ridderstråle, M., Laurila, E., et al. (2003). PGC-1alpha-responsive genes involved in oxidative phosphorylation are coordinately downregulated in human diabetes. Nat. Genet. *34*, 267–273.

41. Dai, Y., Xu, A., Li, J., Wu, L., Yu, S., Chen, J., Zhao, W., Sun, X.J., and Huang, J. (2021). CytoTree: an R/Bioconductor package for analysis and visualization of flow and mass cytometry data. BMC Bioinf. *22*, 138.

42. Pedersen, C.B., Dam, S.H., Barnkob, M.B., Leipold, M.D., Purroy, N., Rassenti, L.Z., Kipps, T.J., Nguyen, J., Lederer, J.A., Gohil, S.H., et al. (2022). cyCombine allows for robust integration of single-cell cytometry datasets within and across technologies. Nat. Commun. *13*, 1698.

43. Garrido-Martín, D., Palumbo, E., Guigó, R., and Breschi, A. (2018). ggsashimi: Sashimi plot revised for browser- and annotation-independent splicing visualization. PLoS Comput. Biol. *14*, e1006360.

44. Nakao, N., Hiraiwa, N., Yoshiki, A., Ike, F., and Kusakabe, M. (1998). Tenascin-C promotes healing of Habu-snake venom-induced glomerulonephritis: studies in knockout congenic mice and in culture. Am. J. Pathol. *152*, 1237–1245.

45. Koyama, Y., Kusubata, M., Yoshiki, A., Hiraiwa, N., Ohashi, T., Irie, S., and Kusakabe, M. (1998). Effect of tenascin-C deficiency on chemically induced dermatitis in the mouse. J. Invest. Dermatol. *111*, 930–935.

46. Matsuda, A., Yoshiki, A., Tagawa, Y., Matsuda, H., and Kusakabe, M. (1999). Corneal wound healing in tenascin knockout mouse. Invest. Ophthalmol. Vis. Sci. *40*, 1071–1080.

47. Uchihara, T., Miyake, K., Yonemura, A., Komohara, Y., Itoyama, R., Koiwa, M., Yasuda, T., Arima, K., Harada, K., Eto, K., et al. (2020). Extracellular Vesicles from Cancer-Associated Fibroblasts Containing Annexin A6 Induces FAK-YAP Activation by Stabilizing beta1 Integrin, Enhancing Drug Resistance. Cancer Res. *80*, 3222–3235.

STAR★METHODS

KEY RESOURCES TABLE

REAGENT or RESOURCE	SOURCE	IDENTIFIER
Antibodies		
Alexa Fluor 647 Rat IgG1, kappa isotype Ctrl	BioLegend	Cat# 400418; RRID:AB_389341
Alexa Fluor(R) 647 anti-mouse CD138 (Syndecan-1)	BioLegend	Cat# 142526; RRID:AB_2566239
Alexa Fluor(R) 647 anti-mouse/human CD324 (E-Cadherin)	BioLegend	Cat# 147308; RRID:AB_2563955
Alexa Fluor® 647 Rat IgG2a, κ Isotype Ctrl Antibody	BioLegend	Cat# 400526; RRID:AB_2864284
Alpha-Smooth Muscle Actin Monoclonal Antibody (1A4)	Thermo Fisher Scientific	Cat# 14-9760-82; RRID:AB_2572996
Anti-alpha smooth muscle Actin antibody	Abcam	Cat# ab5694; RRID:AB_2223021
Anti-Calretinin antibody [1F5H1]	Abcam	Cat# ab204990
Anti-Collagen I antibody [EPR22894-89]	Abcam	Cat# ab264074
Anti-GFP antibody	Abcam	Cat# ab13970; RRID:AB_300798
Anti-Human CD11b/Mac-1 (ICRF44)-167Er	Fluidigm	Cat# 3167011B; RRID:AB_2810974
Anti-Human CD14 (RMO52)-148ND	Fluidigm	Cat# 3148010B; RRID:AB_2858228
Anti-Human CD16 (3G8)-209BiAnti-Human CD16 (3G8)-209Bi	Fluidigm	Cat# 3209002B; RRID:AB_2756431
Anti-Human CD163 (GHI/61) Antibody	Fluidigm	Cat# 3154007B; RRID:AB_2661797
Anti-Human CD181/CXCR1 (8F1/CXCR1)	Fluidigm	Cat# 3142009B
Anti-Human CD182/CXCR2 (5E8/CXCR2)-147Sm	Fluidigm	Cat# 3147010B
Anti-Human CD19 (HIB19)-165Ho	Fluidigm	Cat# 3165025B
Anti-Human CD192/CCR2 (K036C2)-153Eu	Fluidigm	Cat# 3153023B
Anti-Human CD274/PD-L1 (29E.2A3)-156Gd Antibody	Fluidigm	Cat# 3156026B; RRID:AB_2687855
Anti-Human CD279/PD-1 (EH12.2H7)-174Yb	Fluidigm	Cat# 3174020B; RRID:AB_2868402
Anti-Human CD31/PECAM-1	Fluidigm	Cat# 3145004B; RRID:AB_273726
Anti-Human CD326/EpCAM (9C4) Antibody	Fluidigm	Cat# 3141006B; RRID:AB_2687653
Anti-Human CD34 (581)-166Er	Fluidigm	Cat# 3166012B; RRID:AB_2756424
Anti-Human CD4 (RPA-T4)-176Yb	Fluidigm	Cat# 3176010B; RRID:AB_2810247
Anti-Human CD45 (HI30)-89Y	Fluidigm	Cat# 3089003B; RRID:AB_2938863
Anti-Human CD56/NCAM (NCAM16.2)-149Sm	Fluidigm	Cat# 3149021B; RRID:AB_2938638
Anti-Human CD66b (80H3)-152Sm	Fluidigm	Cat# 3152011B; RRID:AB_2661795
Anti-Human CD68 (Y1/82A)	Fluidigm	Cat# 3171011B; RRID:AB_2687637
Anti-Human CD8 (RPA-T8)-146ND	Fluidigm	Cat# 3146001B; RRID:AB_2687641
Anti-Human CD90 (5E10)-159Tb	Fluidigm	Cat# 3159007B; RRID:AB_2893063
Anti-Human HLA-DR (L243)-143ND	Fluidigm	Cat# 3143013B; RRID:AB_2661810
Anti-Human IL-6 (MQ2-13A5)-147Sm	Fluidigm	Cat# 3147002B
Anti-Human PDGFRa (D13C6)-160Gd	Fluidigm	Cat# 3160007A; RRID:AB_2938642
Anti-Human TGFbeta (TW4-6H10)-163Dy	Fluidigm	Cat# 3163010B
Anti-Human TNFa (Mab11)-152Sm	Fluidigm	Cat# 3152002B; RRID:AB_2895145
Anti-Tenascin C antibody [SPM319]	Abcam	Cat# ab212463
APC/Fire(TM) 750 anti-human CD90 (Thy1)	BioLegend	Cat# 328138; RRID:AB_2734314
APC/Fire™ 750 Mouse IgG1, κ Isotype Ctrl (MOPC-21)	BioLegend	Cat# 400195; RRID:AB_2942001
Calretinin antibody	Proteintech	Cat# 12278-1-AP; RRID:AB_2228338

(*Continued on next page*)

Continued

REAGENT or RESOURCE	SOURCE	IDENTIFIER
Cytokeratin, pan Antibody (AE-1/AE-3) [PE]	Novus	Cat# NBP2-33200PE
EpCAM (VU1D9) Mouse	Cell Signaling Technology	Cat# 2929S
FAP Monoclonal Antibody (F11-24)	Thermo Fisher Scientific	Cat# BMS168; RRID:AB_10597443
FITC Mouse IgG1, κ Isotype Ctrl (FC) Antibody	BioLegend	Cat# 400109; RRID:AB_2861401
G-CSF Antibody (7E4F7)	Novus	Cat# NBP2-52447
Goat anti-Chicken IgY (H + L) Secondary Antibody, Alexa Fluor™ 488	Thermo Fisher Scientific	Cat# A-11039; RRID:AB_2534096
Goat anti-Mouse IgG (H + L) Cross-Adsorbed Secondary Antibody, Alexa Fluor™ 568	Thermo Fisher Scientific	Cat# A-11004; RRID:AB_2534072
Goat anti-Rabbit IgG (H + L) Cross-Adsorbed Secondary Antibody, Alexa Fluor™ 594	Thermo Fisher Scientific	Cat# A-11012; RRID:AB_2534079
Goat anti-Rabbit IgG (H + L) Cross-Adsorbed Secondary Antibody, Alexa Fluor™ 647	Thermo Fisher Scientific	Cat# A-21244; RRID:AB_2535812
Goat anti-Rat IgG (H + L) Cross-Adsorbed Secondary Antibody, Alexa Fluor™ 488	Thermo Fisher Scientific	Cat# A-11006; RRID:AB_2534074
Human alpha-Smooth Muscle Actin Allophycocyanin MAb (Cl 1A4)	R and D Systems	Cat# IC1420A; RRID:AB_10890600
Human CXCL1/2/3/GRO Pan Specific MAb (Clone 29702)	R and D Systems	Cat# MAB2761; RRID:AB_2087565
Human CXCL5/ENA-78 MAb (Clone 33170)	R and D Systems	Cat# MAB654; RRID:AB_2245472
Human IL-1 beta/IL-1F2 MAb (Clone 8516)	R and D Systems	Cat# MAB201; RRID:AB_358006
Human M-CSF MAb (Clone 26786)	R and D Systems	Cat# MAB2161; RRID:AB_2085063
Human Syndecan-1 MAb (Clone 359103)	R and D Systems	Cat# MAB2780; RRID:AB_2182840
Human VEGF Antibody	R and D Systems	Cat# MAB2932-100
Human/Mouse Tenascin C MAb (Clone 578)	R and D Systems	Cat# MAB2138; RRID:AB_2203818
IL-8 (1–77) (CXCL8) Monoclonal Antibody (NAP II)	Thermo Fisher Scientific	Cat# BMS136; RRID:AB_10609347
iNOS Monoclonal Antibody (4E5)	Thermo Fisher Scientific	Cat# MA5-17139; RRID:AB_2538610
Mouse IgG1, kappa L Chain Isotype Control	Novus	Cat# NBP1-43778; RRID:AB_10646942
pan Cytokeratin antibody [AE1/AE3]	Abcam	Cat# ab80826; RRID:AB_1640401
pan Cytokeratin antibody [C-11]	Abcam	Cat# ab7753; RRID:AB_306047
PerCP/Cy5.5 Mouse IgG1, κ Isotype Ctrl Antibody	BioLegend	Cat# 400149; RRID:AB_893680
PerCP/Cyanine5.5 anti-human CD31	BioLegend	Cat# 303131; RRID:AB_2566174
Purified anti-human Arginase I	BioLegend	Cat# 369702; RRID:AB_2571898
Purified anti-human CD105	BioLegend	Cat# 323202; RRID:AB_755954
Purified anti-human CD15 (SSEA-1)	BioLegend	Cat# 323002; RRID:AB_756008
Purified anti-human CD206 (MMR) (Maxpar(R) Ready)	BioLegend	Cat# 321127; RRID:AB_2563729
Purified anti-human CD29	BioLegend	Cat# 303002; RRID:AB_314318
Purified anti-human CD3 (Maxpar(R) Ready)	BioLegend	Cat# 300443; RRID:AB_2562808
Purified anti-human CD325 (N-Cadherin)	BioLegend	Cat# 350802; RRID:AB_10662387
Purified anti-human CD33 (Maxpar(R) Ready)	BioLegend	Cat# 303419; RRID:AB_2562818
Purified anti-human CD54	BioLegend	Cat# 353102; RRID:AB_11204426
Purified anti-human CD73 (Ecto-5′-nucleotidase)	BioLegend	Cat# 344002; RRID:AB_2154067
Purified anti-human GM-CSF (Maxpar(R) Ready)	BioLegend	Cat# 502315; RRID:AB_2563770

(*Continued on next page*)

Continued

REAGENT or RESOURCE	SOURCE	IDENTIFIER
Purified anti-human Ki-67 (Maxpar(R) Ready)	BioLegend	Cat# 350523; RRID:AB_2562838
Purified anti-human MCP-1	BioLegend	Cat# 502602; RRID:AB_315241
Purified anti-mouse CD138 (Syndecan-1)	BioLegend	Cat# 142502; RRID:AB_10965646
Purified anti-mouse/human CD44 (Maxpar(R) Ready)	BioLegend	Cat# 103051; RRID:AB_2562799
Rabbit Anti-Human EpCAM Polyclonal Antibody, Unconjugated	Abcam	Cat# ab71916; RRID:AB_1603782
Rat Anti-Human Mesothelin Monoclonal antibody, Unconjugated, Clone 420411	R and D Systems	Cat# MAB32652; RRID:AB_2147798
Recombinant Anti-CDKN2A/p16INK4a antibody [EPR1473]	Abcam	Cat# ab186932; RRID:AB_2895712
Tenascin-C (EGF Like Domain) (4F10TT) Anti-Human Mouse IgG MoAb	IBL	Cat# 10337; RRID:AB_494663
Vimentin Monoclonal Antibody (VI-RE/1)	Thermo Fisher Scientific	Cat# MA1-19319; RRID:AB_1088255
Biological samples		
Ascites fluid from patients	This paper	N/A
Peritoneal dissemination tissue from patients	This paper	N/A
Chemicals, peptides, and recombinant proteins		
Recombinant human TGF-β1	PeproTech	Cat# 100-21C
Recombinant human IL-1β	Miltenyi Biotech	Cat# 130-093-895
VersaLyse Lysing Solution	Beckman Coulter	Cat# A09777
Cell-ID Cisplatin	Fluidigm	Cat# 201198
Human TruStain FcX™	BioLegend	Cat# 422301
Maxpar® Fix I Buffer	Fluidigm	Cat# 201065
Maxpar® Perm-S Buffer	Fluidigm	Cat# 201066
Cell-ID Intercalator-Ir	Fluidigm	Cat# 201192A
EQ Calibration Beads	Fluidigm	Cat# 201078
PKH26	Sigma–Aldrich	Cat# MINI26-1KT
Lipofectamine® RNAiMAX Transfection Reagent	Thermo Fisher Scientific	Cat# 13778-150
Bovine serum albumin	Wako	Cat# 01015094
Histofine antigen retrieval solution (pH 9.0)	Nichirei bioscience	Cat# 415211
Hoechst 33342	Dojindo	Cat# 346-07951
4% paraformaldehyde	Wako	Cat# 163-20145
fetal bovine serum	Capricorn Scientific	Cat# FBS-LE-12A
Opti-MEM	Thermo Fisher Scientific	Cat# 31985-070
RPMI-1640	Wako	Cat# 189-02145
Critical commercial assays		
RNeasy Mini Kit	QIAGEN	Cat# 74106
RNase-Free DNase Set	QIAGEN	Cat# 79254
Human TGF-beta 1 Quantikine ELISA Kit	R and D Systems	Cat# DB100B
Human IL-1 beta/IL-1F2 Quantikine HS ELISA Kit	R and D Systems	Cat# HSLB00D
Human Tenascin C ELISA Kit	Abcam	Cat# ab277081
LEGENDplex Human Proinflammatory Chemokine Panel (13-plex)	BioLegend	Cat# 740985
BD™ Cytometric Bead Array (CBA) Human VEGF Flex Set	BD BioSciences	Cat# 558336
Direct RNA Sequencing Kit	Oxford Nanopore Technologies	Cat# SQK-RNA002

(*Continued on next page*)

Continued

REAGENT or RESOURCE	SOURCE	IDENTIFIER
Deposited data		
RNA sequencing data	This paper	DRA014736
Single-cell RNA-seq data	Wang et al.[1]	EGAS00001004443
Proteomics mass spectrometry data	This paper	PXD037200
RNA-seq data of gastric cancer cells in ascites	Tanaka et al.[3]	GSE162214
Experimental models: Cell lines		
Human: NUGC3	Japanese Collection of Research Bioresources Cell Bank	Cat# JCRB0822; RRID:CVCL_1612
Human: Mesothelial cells	This paper	N/A
Mouse: GAN-KP	Yamasaki et al.[21]	N/A
Mouse: GAN-KPC	This paper	N/A
Mouse: GAN-KPCS	This paper	N/A
Experimental models: Organisms/strains		
C57BL/6 N	CLEA Japan	N/A
Tnc-KO mice (B6. Cg-Tnc<tm1Sia>/Rbrc)	RIKEN Bioresource Research Center	RBRC00169
Oligonucleotides		
Silencer™ Select Negative Control No. 1 siRNA	Thermo Fisher Scientific	Cat# 4390843
Silencer™ Select siRNA TNC s7068	Thermo Fisher Scientific	Cat# 4390824, Assay ID# s7068
Silencer™ Select siRNA TNC s7069	Thermo Fisher Scientific	Cat# 4390824, Assay ID# s7069
Alt-R® CRISPR–Cas9 crRNA: Mm.Cas9.CDH1.1.AA/AltR1/rGrG rArGrC rUrGrA rCrArA rArCrC rCrCrC rCrGrU rGrUrU rUrUrA rGrArG rCrUrA rUrGrC rU/AltR2/	Integrated DNA Technologies	Cat# Mm.Cas9.CDH1.1.AA
Alt-R® CRISPR–Cas9 crRNA: Mm.Cas9.CDH1.1.AB/AltR1/rCrG rUrCrU rGrUrC rGrCrC rArCrU rUrUrG rArArU rGrUrU rUrUrA rGrArG rCrUrA rUrGrC rU/AltR2/	Integrated DNA Technologies	Cat# Mm.Cas9.CDH1.1.AB
Alt-R® CRISPR–Cas9 crRNA: Mm.Cas9.CDH1.1.AC/AltR1/rUrC rUrGrA rGrArC rCrUrG rGrGrU rArCrA rCrGrC rGrUrU rUrUrA rGrArG rCrUrA rUrGrC rU/AltR2/	Integrated DNA Technologies	Cat# Mm.Cas9.CDH1.1.AC
Alt-R® CRISPR–Cas9 tracrRNA, ATTO 550	Integrated DNA Technologies	N/A
Invitrogen TrueGuide sgRNA Modified, custom: Sdc1_C1 ACUGCCAAUCAGCUUCCCGC	Thermo Fisher Scientific	Cat# GREPUFC
Invitrogen TrueGuide sgRNA Modified, custom: Sdc1_C1 GUGCCGCCACCCUCCACACG	Thermo Fisher Scientific	Cat# GRFVMY9
Recombinant DNA		
pLVSIN-AcGFP1-N1	Takara	Cat# 6187
Software and algorithms		
Trim Galore (v0.6.7)	Krueger et al.	https://github.com/FelixKrueger/TrimGalore
STAR (v2.7.9a)	Dobin et al.[38]	https://github.com/alexdobin/STAR
RSEM (v1.3.3)	Li et al.	https://github.com/deweylab/RSEM
Subio Platform (ver. 1.23.5853)	Subio	https://www.subioplatform.com/
GSEA software (v. 4.1.0)	Subramanian, Tamayo et al.[39] Mootha, Lindgren et al.[40]	https://www.gsea-msigdb.org/gsea/index.jsp
Cytobank software (9.4)	Beckman Coulter	https://premium.cytobank.org/

(*Continued on next page*)

Continued

REAGENT or RESOURCE	SOURCE	IDENTIFIER
CytoTree (ver 1.2.0)	Dai et al.[41]	https://github.com/JhuangLab/CytoTree
cyCombine (v0.2.5)	Pedersen et al.[42]	https://github.com/biosurf/cyCombine
ggcorrplot2 (0.1.2)	Jun Cai	https://github.com/caijun/ggcorrplot2
LEGENDplex™ Data Analysis Software Suite (Cloud-based Program)	BioLegend	https://legendplex.qognit.com/user/login?next=workflow.workflow
IncuCyte S3 (2019B Rev)	Sartorius	N/A
BZ-H3A software	Keyence	N/A
FlowJo (v10.8.0)	BD BioSciences	https://www.flowjo.com/solutions/flowjo/downloads
CellChat (v.1.4.0)	Jin et al.[16]	https://github.com/sqjin/CellChat
Guppy (4.0.14)	Oxford Nanopore Technologies	https://nanoporetech.com/
wf-isoforms pipeline	Oxford Nanopore Technologies	https://github.com/epi2me-labs/wf-isoforms
ggsashimi (v1.1.5)	Garrido-Martin et al.[43]	https://github.com/guigolab/ggsashimi
R (4.1.2)	R Core Team	https://www.r-project.org/
MinKNOW (3.6.5)	Oxford Nanopore Technologies	https://nanoporetech.com/

RESOURCE AVAILABILITY

Lead contact

Further information and requests for resources and reagents should be directed to and will be fulfilled by the Lead Contact, Takatsugu Ishimoto (takatsugu.ishimoto@jfcr.or.jp)

Materials availability

Materials generated in this study will be made available upon reasonable request.

Data and code availability

All data are provided with the article. RNA-seq data were deposited in DRA: DRA014736. Single-cell RNA-seq data have been deposited in the European Genome-Phenome Archive: EGAS00001004443. Proteomics mass spectrometry data were deposited in the ProteomeXchange Consortium via the jPOST repository: PXD037200.

This paper does not report the original code. Any additional information required to reanalyze the data reported in this paper is available from the lead contact upon request.

EXPERIMENTAL MODEL AND STUDY PARTICIPANT DETAILS

Patients and tissue samples

Ascites fluid was collected by physicians from patients with gastric cancer (GC) or liver cirrhosis (LC) at Kumamoto University and Kanamecho Hospital as described previously[27] after obtaining informed consent from each patient (Table S1). The peritoneal dissemination sample was surgically resected at Kumamoto University. This study was approved by the Medical Ethics Committee of Kumamoto University (Approval Number: 1277).

Cell lines and cell culture

We obtained the human GC cell line NUGC-3 from the Japanese Collection of Research Bioresources Cell Bank. The mouse GC cell line GAN-KP was provided by Dr. Osamu Nagano at Keio University. GC cell lines were cultured in Roswell Park Memorial Institute (RPMI) 1640 medium (Wako, Osaka, Japan) supplemented with 10% fetal bovine serum (FBS) (Capricorn Scientific, Ebsdorfergrund, Germany) (hereafter referred to as normal medium) at 37°C with 5% CO_2. Mesothelial cells were obtained by culturing cells from ascites of GC patients. Briefly, the ascites samples were passed through a 70 μm filter (Falcon, Corning, NY) and centrifuged at 1,500 rpm for 15 min. The supernatants were collected and stored at −80°C for proteomics or ELISA experiments. Cell pellets were resuspended in 1xACK buffer (Thermo Fisher Scientific, Waltham, MA) and incubated at room temperature for 5 min to lyse red blood cells. After washing with PBS and counting the cells, the cells were cultured in normal medium. Mesothelial cells were naturally selected as they were passaged more than 2 times and stored at −80°C until further use. The purity of the mesothelial cell population was confirmed by flow cytometry.

Animals

Female wild-type C57BL/6N mice were purchased from CLEA Japan (Tokyo, Japan). Female *Tnc*-KO mice (B6. Cg-Tnc$^{tm1Sia/Rbrc}$)[44–46] were obtained from the RIKEN Bioresource Research Center. All mice were housed in a specific-pathogen free (SFP) room under stable temperature and humidity conditions on a 12-h light/dark cycle. Both water and food were supplied *ad libitum*. Mice aged 7–9 weeks were used for experiments. All animal procedures and studies were conducted in accordance with the protocol approved by the Institutional Animal Care and Use Committee at Kumamoto University (Approval Number: A2022-026).

METHOD DETAILS

MMT induction in mesothelial cells

Mesothelial cells were stimulated with normal medium supplemented with 0.5 ng/mL recombinant human TGF-β1 (PeproTech, Rocky Hill, NJ), 2.5 ng/mL recombinant human IL-1β (Miltenyi Biotech, North Rhine-Westphalia, Germany), or a combination of TGF-β1 and IL-1β. Cells cultured in normal medium were used as controls. After 48 h of stimulation, the cells were harvested and subjected to further analysis.

Conditioned medium

The mesothelial cell culture medium was replaced with fresh FBS-free RPMI 1640 medium supplemented with TGF-β1, IL-1β, or a combination as described above. After 48 h, CM was collected from each group and passed through a 0.22 μm filter (Millipore Sigma, Burlington, MA). The CM was stored at −80°C until further use.

Mass cytometry

CyTOF analysis was performed as described previously.[27] Briefly, cells from ascites samples were collected by centrifugation, and red blood cells were lysed by VersaLyse Lysing Solution (Beckman Coulter, Brea, CA). After washing with PBS and counting, 3 x 10^6 cells per antibody panel were labeled with Cell-ID Cisplatin (Fluidigm, South San Francisco, CA) and blocked with Human TruStain FcX (BioLegend). A cocktail of cell surface antigen-targeting antibodies was added, and the samples were incubated for 30 min. Cells were fixed and permeabilized with Maxpar Fix I Buffer and Maxpar Perm-S Buffer (Fluidigm) and stained with a cocktail of antibodies against cytoplasmic antigens for 1 h. After methanol treatment, a nuclear antigen targeting antibody mix was applied and incubated for 1 h. Cells were then barcoded with Cell-ID Intercalator-Ir (Fluidigm) at RT for 1 h, washed with Maxpar Water (Fluidigm), and resuspended with 10% EQ Calibration Beads (Fluidigm). Data were acquired on a Helios CyTOF system (Fluidigm). The antibody panels used for CyTOF analyses in this study are listed in Table S2.

Mass cytometry data analysis

Mass cytometry data were analyzed using Cytobank software. First, the collected data were manually gated to remove calibration beads, debris and dead cells (Figure S1A). For LC and GC ascites analysis using antibody panel 1 (Figure 1), cells were clustered using the FlowSOM algorithm and annotated by cell marker expression using Cytobank. The t-distributed stochastic neighbor embedding (t-SNE) analysis was performed to visualize the cell population and marker expression. For MMT-induced mesothelial cell analysis (Figures 2C–2E) and mesothelial cell analysis in GC ascites (Figures 2F–2J) using antibody panel 2, CD45(−)/EpCAM(−) cells were clustered by the FlowSOM algorithm using CytoTree[41] (ver 1.2.0) and visualized using t-SNE plots. The MMT-induced mesothelial cell (Ctrl-Meso and MMT-meso) and GC ascites mesothelial cell data were combined with batch correction followed by dimensionality reduction and visualization by uniform manifold approximation and projection (UMAP) by using the cyCombine[42] R package (https://github.com/biosurf/cyCombine). For immune cell analysis in LC and GC ascites using antibody panel 3 (Figures 3D–3F), $CD45^+$ cells were clustered by the FlowSOM algorithm and annotated based on cell marker expression, and the t-SNE method was used to visualize the data using CytoTree. For analyses of the correlation between the proportions of each cell cluster in GC ascites (Figure 3G), the proportion of each cluster in the total cell population was calculated as (the percentage of parent clusters {i.e., $CD45^+$, $EpCAM^+$, and CD45(−)/EpCAM(−)} in total cells) x (the percentage of progeny clusters in parent clusters). Spearman's correlation coefficients were summarized as a correlation matrix by ggcorrplot2.

Single-cell RNA-Sequencing (scRNA-seq) analysis

Previously deposited datasets were downloaded from the European Genome-phenome Archive repository: EGAS00001004443. The peritoneal metastasis of the GC cohort contained 23559 cells from 20 patients. Seurat, cowplot and dplyr were installed in R Studio to explore QC metrics, normalize data and identify cluster signature genes. "Vlnplot" functions were used to reveal profiles of genes of interest.

Bulk RNA-seq for MMT-induced mesothelial cells

Mesothelial cells from the ascites of patients (n = 3) were stimulated with a vehicle control, TGF-β1, IL-1β, or a combination of TGF-β1 and IL-1β for 48 h as described above. After 48 h of culture, total RNA of cells from each group was extracted and purified using an RNeasy Mini Kit (QIAGEN, Hilden, Germany) and RNase-Free DNase Set (QIAGEN) according to the manufacturer's instructions. The quality of the RNA was assessed by a 2100 Bioanalyzer (Agilent, Santa Clara, CA), and only samples

with an RNA integrity number >8.0 were used for library preparation. Single-indexed libraries were prepared using the TruSeq Stranded mRNA Library Prep Kit LT (Illumina, San Diego, CA), and paired-end sequencing was performed by NextSeq500 (Illumina) with a high-output flow cell. Adapter trimming and quality control of the FASTQ data were performed with Trim Galore (v0.6.7). The filtered reads were mapped to the Ensembl human GRCh38.p13 reference genome using STAR (v2.7.9a), and RSEM (v1.3.3) was used to estimate gene expression levels. DEGs were identified using the Subio Platform (ver. 1.23.5853). Genes with less than 20 counts were excluded, and genes with q value <0.05 and $\log_2$ fold change >3.0 were considered DEGs. Transcript per million (TPM) values were used for GSEA to identify enriched REACTOME pathways by GSEA software (v. 4.1.0) with default settings.

ELISA

The concentrations of TGF-β1, IL-1β, and TNC in ascites from patients were measured using a Human TGF-beta 1 Quantikine ELISA Kit (R&D Systems, Minneapolis, MN), Human IL-1 beta/IL-1F2 Quantikine HS ELISA Kit (R&D Systems), and Human Tenascin C ELISA Kit (Abcam) according to the manufacturer's protocols. Data were acquired by a Synergy H1 (BioTeK, Winooski, VT).

Chemokine bead array

To quantify the chemokines and VEGF in the ascites samples from patients with GC (n = 20) or LC (n = 10), bead-based immunoassays were performed using the LEGENDplex Human Proinflammatory Chemokine Panel (13-plex) (BioLegend, San Diego, CA) and Human VEGF Flex Set (BD BioSciences, Franklin Lakes, NJ) according to the manufacturer's instructions. The samples were analyzed by a BD FACSVerse (BD Biosciences). Data from the Human VEGF Flex Set were analyzed by Microsoft Excel. Data obtained by using the Human Proinflammatory Chemokine Panel were analyzed by cloud-based LEGENDplex Data Analysis Software.

Proteomic analysis

Proteomic analysis by mass spectrometry was performed to characterize proteins in ascites samples from patients with GC (n = 7) or LC (n = 3) at the Liaison Laboratory Research Promotion Center at Kumamoto University as described previously.[47] Peptides were analyzed on an Advance UHPLC system (Michrom Bioscience, Auburn, CA) and a Q Exactive mass spectrometer (Thermo Fisher Scientific), and the raw mass spectrum data were processed using Xcalibur (Thermo Fisher Scientific). Each protein score in ascites from LC and GC patients was compared by Welch's t test. Proteins enriched in either LC or GC ascites with $p < 0.05$ were considered differentially expressed proteins and are summarized in a heatmap in Figure 4C.

Bioinformatic cell–cell communication analysis

We analyzed our RNA-seq data for MMT-induced mesothelial cells together with previously reported RNA-seq data of gastric cancer cells in ascites.[3] In the dataset of Tanaka et al., cancer cells in ascites were purified by either negative selection using CD45 microbeads or positive selection using EpCAM microbeads for analyses, and we downloaded only FASTQ files from RNA-seq for $EpCAM^+$ cancer cells from the Gene Expression Omnibus (GSE162214). These FASTQ files were processed with our FASTQ files from RNA-seq for mesothelial cells. STAR (v2.7.9a) and RSEM (v1.3.3) were used to obtain a normalized gene expression matrix for the integrated dataset. The CellChat[16] R package (v.1.4.0) was used to infer and visualize the intercellular communication among mesothelial cells and cancer cells in peritoneal ascites.

Spheroid assay

The human GC cell line NUGC-3 was labeled with *Aequorea coerulescens* green fluorescent protein (AcGFP1) by lentiviral transduction of pLVSIN-AcGFP1-N1 (Takara Bio, Siga, Japan).

For the spheroid formation assay, NUCG-3-AcGFP1 cells were seeded in a low-attachment 96-well plate (IWAKI, Shizuoka, Japan) at a density of 5×10^3 cells per well and cultured for 48 h to form spheroids. The spheroids were then stimulated with fresh normal medium, GC patient ascites, or normal medium containing CM from the control or combination group described above at a 1:1 ratio. After 24 h of stimulation, the GFP-positive area was measured every hour by the hybrid cell count function in a BZ-X700 fluorescence microscope (Keyence, Osaka, Japan).

For the spheroid attachment assay, NUCG-3-AcGFP1 cells were seeded in a low-attachment 96-well plate at a density of 1×10^3 cells per well. In parallel, mesothelial cells were cultured with normal medium (Ctrl-Meso) or normal medium supplemented with 0.5 ng/mL TGF-β1 and 2.5 ng/mL IL-1β (MMT-Meso). After 48 h, the spheroids of NUCG-3-AcGFP1 cells were transferred to the wells of Ctrl-Meso or MMT-Meso cells stained with PKH26 (Sigma–Aldrich) and cocultured in normal medium. The mesothelial cell cleared area was measured by IncuCyte S3 (Sartorius, Gottingen, Germany) every 3 h for up to 48 h. After 48 h of coculture, the protein expression of EpCAM and TNC was evaluated by fluorescent immunocytochemistry.

Small interfering RNA transfection

TNC expression was suppressed by transfecting cells with predesigned Silencer Select siRNAs against TNC (s7068 and s7069, Cat# 4390824, Thermo Fisher Scientific), and a nontargeting siRNA (#4390843, Thermo Fisher Scientific) was used as the negative control. Mesothelial cells were plated in a 12-well plate at 2.5×10^4 cells per well. Twenty-four hours after plating, the cells were transfected with 5 nM TNC or control siRNA using Lipofectamine RNAiMAX Transfection Reagent (Thermo Fisher Scientific) according to the

manufacturer's instructions. After 12 h of transfection, the cells were changed to fresh RPMI 1640 medium supplemented with TGF-β1 and IL-1β for MMT induction and subjected to a spheroid attachment assay.

Immunohistochemistry

Formalin-fixed, paraffin-embedded sections of peritoneal dissemination samples from a patient with GC or mice were sectioned to 3 μm and stained with hematoxylin-eosin (H&E) or subjected to fluorescent immunohistochemistry. Briefly, the sections were deparaffinized, rehydrated and microwaved in Histofine antigen retrieval solution (pH 9.0) (Nichirei Bioscience, Tokyo, Japan) for antigen retrieval. The sections were then blocked with 3% bovine serum albumin (BSA) (Wako) for 10 min at RT. Primary antibodies were diluted in 1.5% BSA and incubated for 1 h at RT or overnight at 4°C. After washing with Tween-PBS, secondary antibodies diluted in 1.5% BSA were applied for 30 min at RT, and nuclei were stained with Hoechst 33342 (Dojindo, Kumamoto, Japan). Images were captured with a VS120 fluorescence microscope (Olympus, Tokyo, Japan). Once the images were obtained, the coverslips were removed, and the antibody complex on the slides was stripped by microwave treatment. The sections were then blocked, incubated with antibodies, and counterstained with Hoechst 33342 as described above. The wsireg python package (https://github.com/NHPatterson/wsireg) was used to perform registration of the acquired images. The antibodies used are listed in Table S3.

Immunocytochemistry

Cells in the plates were fixed with 4% paraformaldehyde (Wako) for 10 min at RT. After washing with PBS, the cells were permeabilized with 0.1% Triton X-100/PBS (Wako) for 5 min at RT and washed with PBS again. The cells were then blocked with 5% skim milk for 30 min at RT and incubated with primary antibodies diluted in 1% BSA overnight at 4°C. Secondary antibodies in 1% BSA were applied for 1 h at RT, and nuclei were stained with DAPI. Images of samples were taken by a BZ-X700 fluorescence microscope and analyzed using the hybrid cell count function in BZ-H3A software to quantify integrated intensity. The antibodies used are listed in Table S3.

Generation of *Cdh1*-knockout KP cells by CRISPR–Cas9

Knockout of the *Cdh1* and *Sdc1* genes in GAN-KP cells was performed by using the Alt-R CRISPR–Cas9 System (Integrated DNA Technologies, Coralville, IA). To prepare RNA oligos, 1 μL of 100 μM crRNA targeting each gene designed by Integrated DNA Technologies and 1 μL of 100 μM tracrRNA-ATTO550 were incubated in 98 μL of nuclease-free duplex water at 95°C for 5 min. Ribonucleoprotein (RNP) complexes were formed by combining 1.5 μL of 1 μM RNA oligo and 1.5 μL of 1 μM Alt-R *S.p.* Cas9 nuclease in 22 μL of Opti-MEM (Thermo Fisher Scientific) and incubating at room temperature (RT) for 5 min. To prepare transfection complexes, 25 μL of each RNP complex was incubated with 1.2 μL of Lipofectamine RNAiMAX Transfection Reagent (Thermo Fisher Scientific) in 23.8 μL of Opti-MEM at RT for 20 min. In parallel, GAN-KP cells were trypsinized and resuspended in normal medium to a concentration of 4.0 x 10^5 cells/mL. After incubation, 50 μL of each transfection complex was added to a 96-well plate (Corning, Corning, NY), and 100 μL of GAN-KP cell suspension was added to each well with the transfection complex. Cells were then incubated at 37°C in a 5% CO_2 incubator for 48 h. *Cdh1* KO cells were purified by FACS based on their E-cadherin expression, and *Sdc1* KO cells were generated by single-cell cloning followed by validation of Sdc1 expression by flow cytometry.

Flow cytometry

Cell suspensions were stained with antibodies (listed in Table S3) for 30 min on ice and washed with PBS containing 2% FBS. The cells were then resuspended in PBS and analyzed with a FACSVerse instrument. Flow cytometry data were analyzed by FlowJo software.

In vivo experiments

To establish peritoneal dissemination models, 10^6 GAN-KP cells, GAN-KPC cells, or GAN-KPCS cells were suspended in 400 μL of PBS and injected intraperitoneally into wild-type or *Tnc*-KO mice. Mice were weighed every 3 days and closely monitored. Three weeks after transplantation, the mice were sacrificed, and tumors and ascites were collected for further analysis.

TNC isoform analysis

We used the MinION Mk1B system (Oxford Nanopore Technologies, Oxford, UK) to perform long-read direct RNA sequencing. Total RNA from mesothelial cells stimulated with a combination of TGF-β1 and IL-1β, which was also used for bulk RNA sequencing, was processed for library preparation using an SQK-RNA002 kit according to the manufacturer's instructions. MinKNOW 3.6.5 was used to sequence the sample, and base calling was performed by Guppy 4.0.14. We used the wf-isoforms pipeline (https://github.com/epi2me-labs/wf-isoforms) to align the reads to the human GRCh38.p13 reference genome and generate a GTF transcript annotation file. The FASTQ files from bulk short-read RNA-seq data of ascites GC tumor cells from the dataset of Tanaka et al. (GSE162214)[3] and mesothelial cells treated with vehicle control or a combination of TGF-β1 and IL-1β were then remapped to the obtained annotation by STAR (v2.7.9a). TNC isoform expression in each cell type was visualized as a Sashimi plot using ggsashimi (v1.1.5).[43]

QUANTIFICATION AND STATISTICAL ANALYSIS

All experiments were repeated at least twice. The sample sizes for each experiment were determined empirically. The data are presented as the mean ± standard deviation. Welch's t test was used to evaluate differences between 2 groups. One-way ANOVA followed by the Tukey–Kramer multiple comparison test was used to compare multiple groups. A two-way repeated measures analysis of variance was performed to compare sphere growth. Spearman's correlation coefficient was used to analyze the correlation between the population of each cell type in malignant ascites. Statistical analysis was performed using R. All p values were two sided, and $p < 0.05$ was considered statistically significant.

Cell Reports, Volume *43*

Supplemental information

Mesothelial cells with mesenchymal features enhance peritoneal dissemination by forming a protumorigenic microenvironment

Atsuko Yonemura, Takashi Semba, Jun Zhang, Yibo Fan, Noriko Yasuda-Yoshihara, Huaitao Wang, Tomoyuki Uchihara, Tadahito Yasuda, Akiho Nishimura, Lingfeng Fu, Xichen Hu, Feng Wei, Fumimasa Kitamura, Takahiko Akiyama, Kohei Yamashita, Kojiro Eto, Shiro Iwagami, Masaaki Iwatsuki, Yuji Miyamoto, Keisuke Matsusaki, Juntaro Yamasaki, Osamu Nagano, Hideyuki Saya, Shumei Song, Patrick Tan, Hideo Baba, Jaffer A. Ajani, and Takatsugu Ishimoto

Supplementary Figures

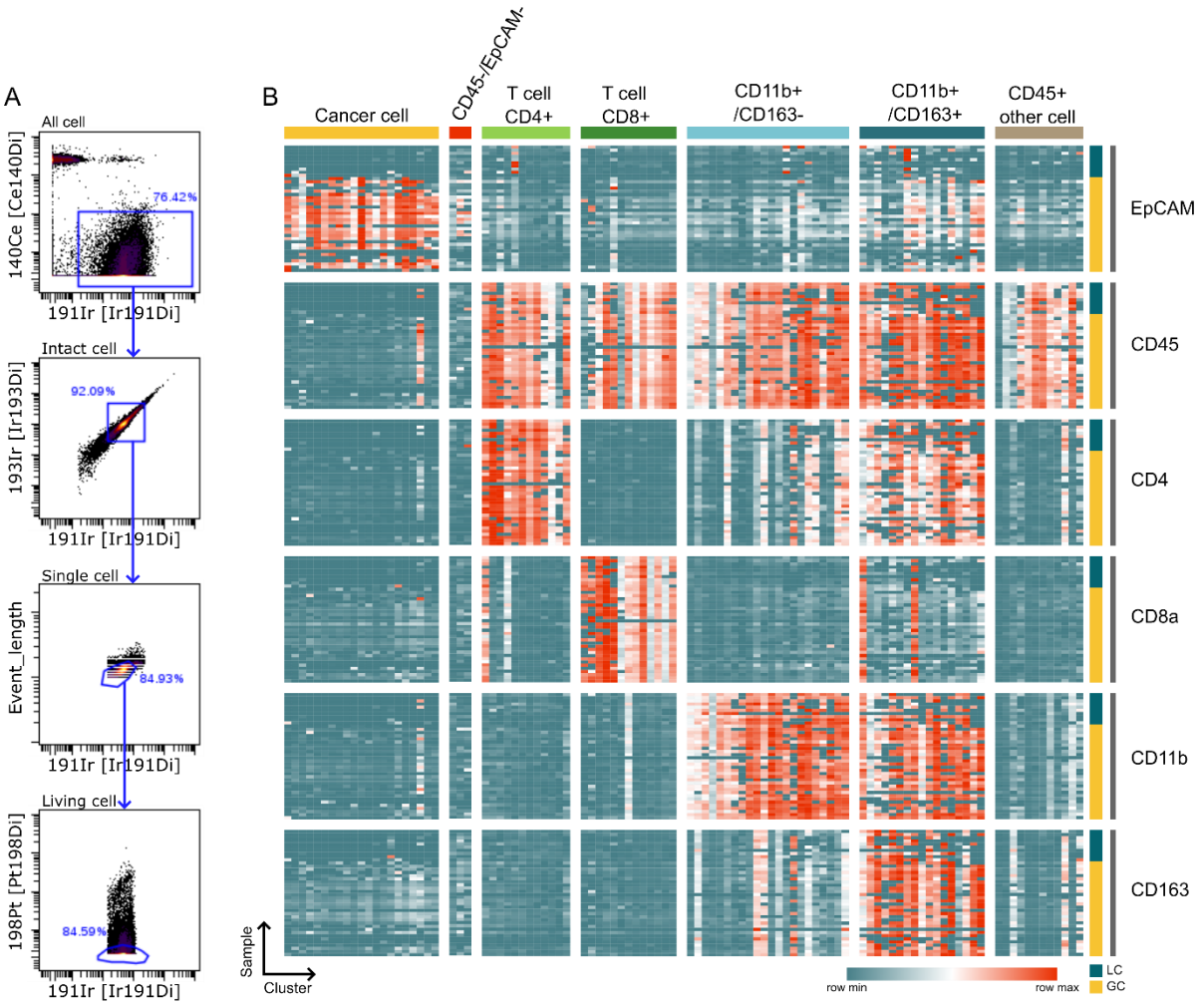

Supplementary Figure 1. Attenuated immune surveillance against tumors and the frequent presence of CD45(-)/EpCAM(-) cells in malignant ascites. (**A**) Gating strategy for mass cytometry analysis of cancer cells and nonmalignant cell subsets in ascites. Intact ascites cells from liver cirrhosis or gastric cancer patients were first gated by 191Ir vs. 140Ce to remove calibration beads. Single live cells were gated based on 193Ir and event length parameters, followed by gating for 198Pt-negative cells. (**B**) Heatmap demonstrating the expression of a cancer cell marker (EpCAM), immune cell marker (CD45), T-cell markers (CD4 and CD8), and myeloid/macrophage markers (CD11b and CD163) in each cell population from the FlowSOM clustering result.

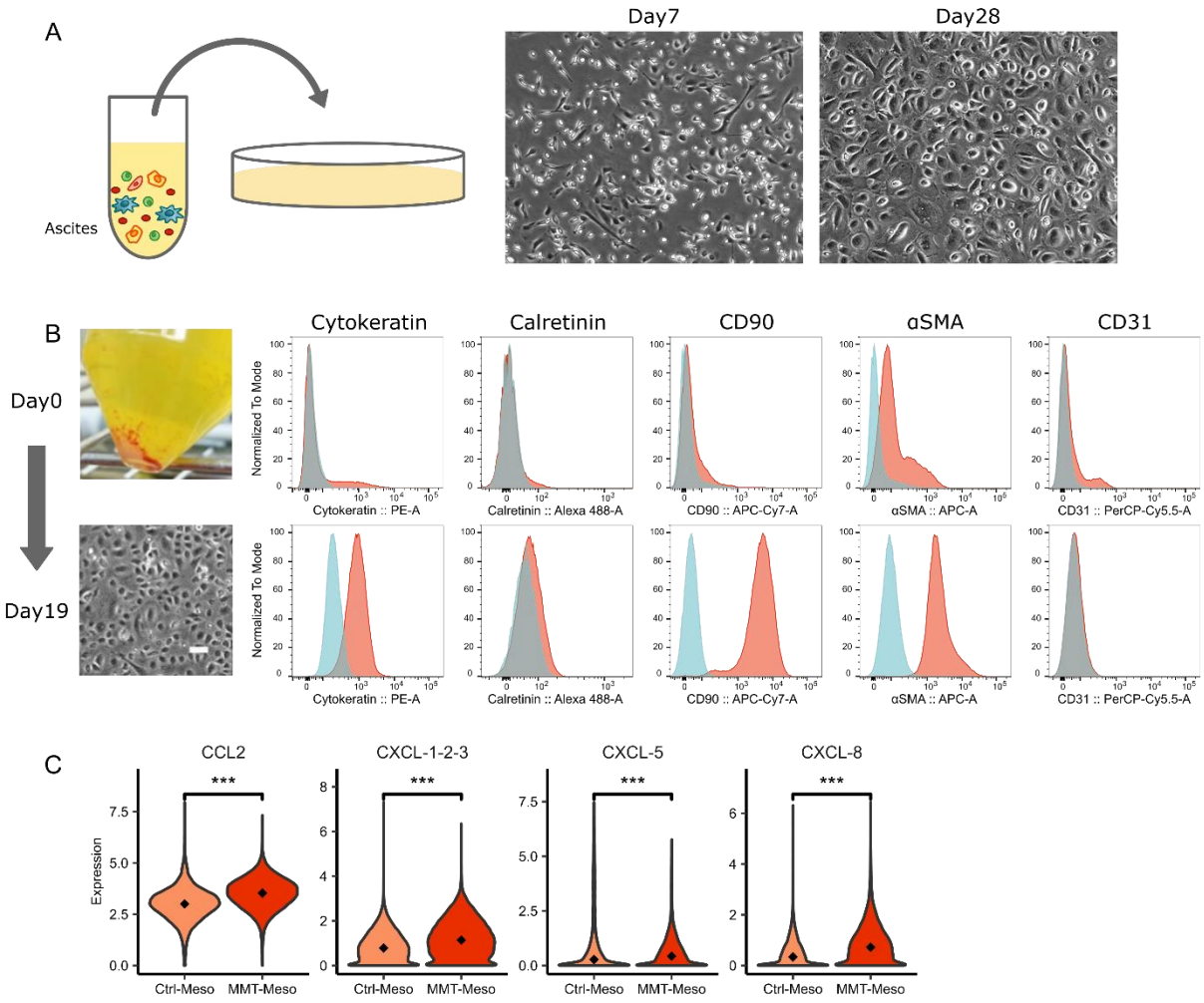

Supplementary Figure 2. Isolation of mesothelial cells from GC ascites. (**A**) Scheme showing ascites cell culture to isolate mesothelial cells. Representative phase-contrast microscopy images of ascites cells 7 days (Day 7) and 28 days (Day 28) after culture are shown. (**B**) The expression of epithelial cell markers (cytokeratin), mesothelial cell markers (calretinin), mesenchymal cell markers (CD90 and αSMA), and endothelial cell markers (CD31) by ascites cells before culture (day 0) and 19 days after culture (day 19) was assessed by flow cytometry, and the data are shown as histograms. The gross appearance of the cell pellet in ascites on Day 0 and representative images of phase-contrast microscopy of ascites cells on Day 19 are shown in the leftmost panel. Scale bar = 100 μm. (**C**) Violin plots showing the expression of CCL2, CXCL1/2/3, CXCL5, and CXCL8 in cells in the Ctrl-Meso and MMT-Meso clusters.

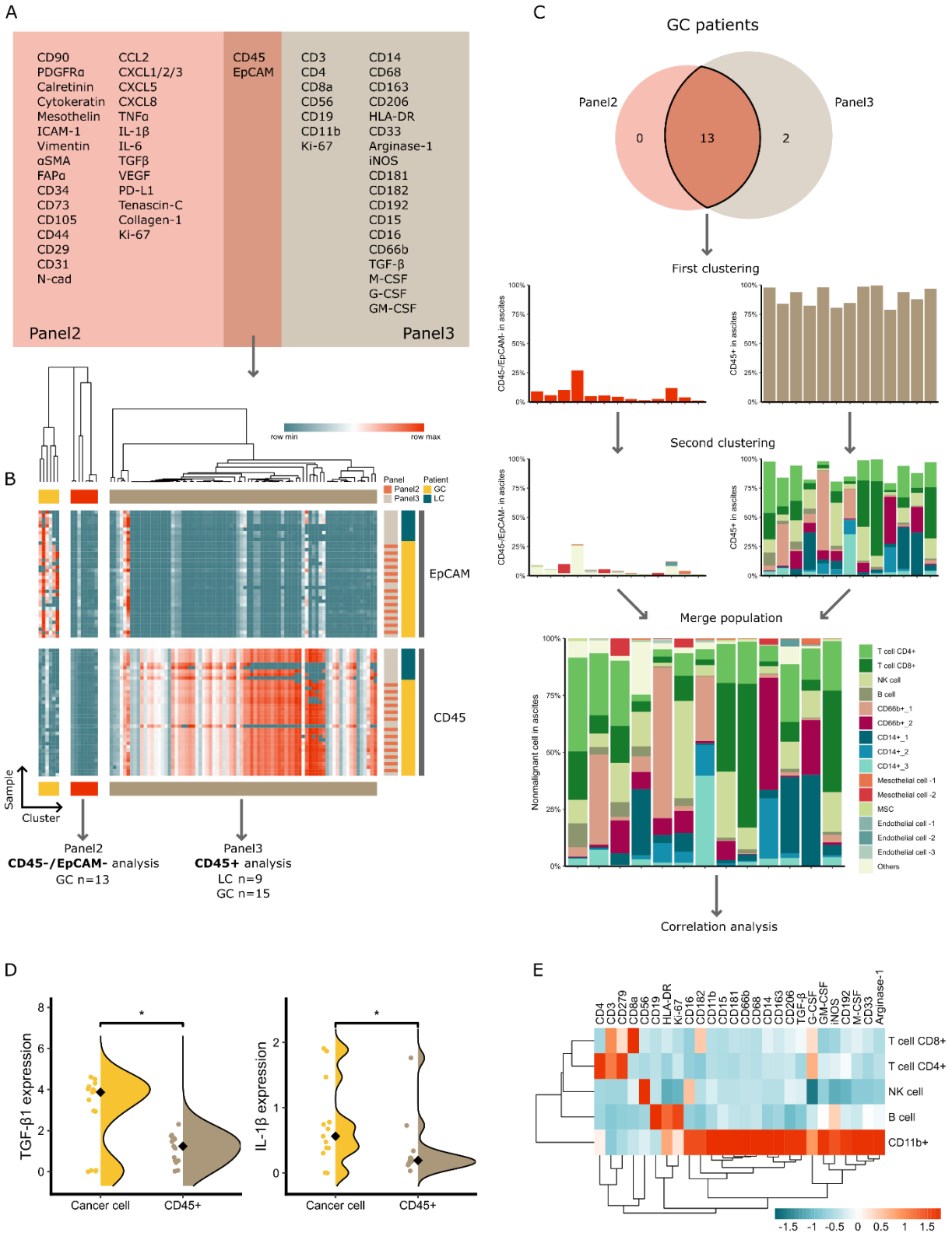
A
CD90
PDGFRα
Calretinin
Cytokeratin
Mesothelin
ICAM-1
Vimentin
αSMA
FAPα
CD34
CD73
CD105
CD44
CD29
CD31
N-cad
CCL2
CXCL1/2/3
CXCL5
CXCL8
TNFα
IL-1β
IL-6
TGFβ
VEGF
PD-L1
Tenascin-C
Collagen-1
Ki-67
CD45
EpCAM
CD3
CD4
CD8a
CD56
CD19
CD11b
Ki-67
CD14
CD68
CD163
CD206
HLA-DR
CD33
Arginase-1
iNOS
CD181
CD182
CD192
CD15
CD16
CD66b
TGF-β
M-CSF
G-CSF
GM-CSF
Panel2
Panel3
B
row min
row max
Panel
Patient
Panel2
Panel3
GC
LC
EpCAM
CD45
Sample
Cluster
Panel2
CD45-/EpCAM- analysis
GC n=13
Panel3
CD45+ analysis
LC n=9
GC n=15
C
GC patients
Panel2
Panel3
0
13
2
First clustering
CD45-/EpCAM- in ascites
CD45+ in ascites
Second clustering
Merge population
Nonmalignant cell in ascites
T cell CD4+
T cell CD8+
NK cell
B cell
CD66b+_1
CD66b+_2
CD14+_1
CD14+_2
CD14+_3
Mesothelial cell -1
Mesothelial cell -2
MSC
Endothelial cell -1
Endothelial cell -2
Endothelial cell -3
Others
Correlation analysis
D
TGF-β1 expression
IL-1β expression
Cancer cell
CD45+
E
CD4
CD3
CD279
CD8a
CD56
CD19
HLA-DR
Ki-67
CD16
CD182
CD11b
CD15
CD181
CD66b
CD68
CD14
CD163
CD206
TGF-β
G-CSF
GM-CSF
iNOS
CD192
M-CSF
CD33
Arginase-1
T cell CD8+
T cell CD4+
NK cell
B cell
CD11b+

Supplementary Figure 3. Mass cytometry data analysis and clustering of cell populations. (**A**) List of target antigens in panels 2 and 3 for mass cytometry analysis. (**B**) Heatmap demonstrating EpCAM and CD45 expression in FlowSOM clusters in each sample. Cells in the EpCAM(-)/CD45(-) population were further analyzed using panel 2, and those allocated to the CD45+ population were further analyzed using panel 3. (**C**) Analysis of each cell cluster proportion for correlation analysis in Figure 3G. To merge subclusters of EpCAM(-)/CD45(-) and CD45+ cell populations, the percentages of each subcluster in the total cells were calculated as (the percentage of parent clusters in total cells) x (the percentage of subclusters in parent clusters). (**D**) Half violin plots showing the expression of TGF-β1 in cancer cells and CD45+ cells in ascites from GC patients. (**E**) Heatmap showing the expression of markers in panel 3 by each immune cell cluster.

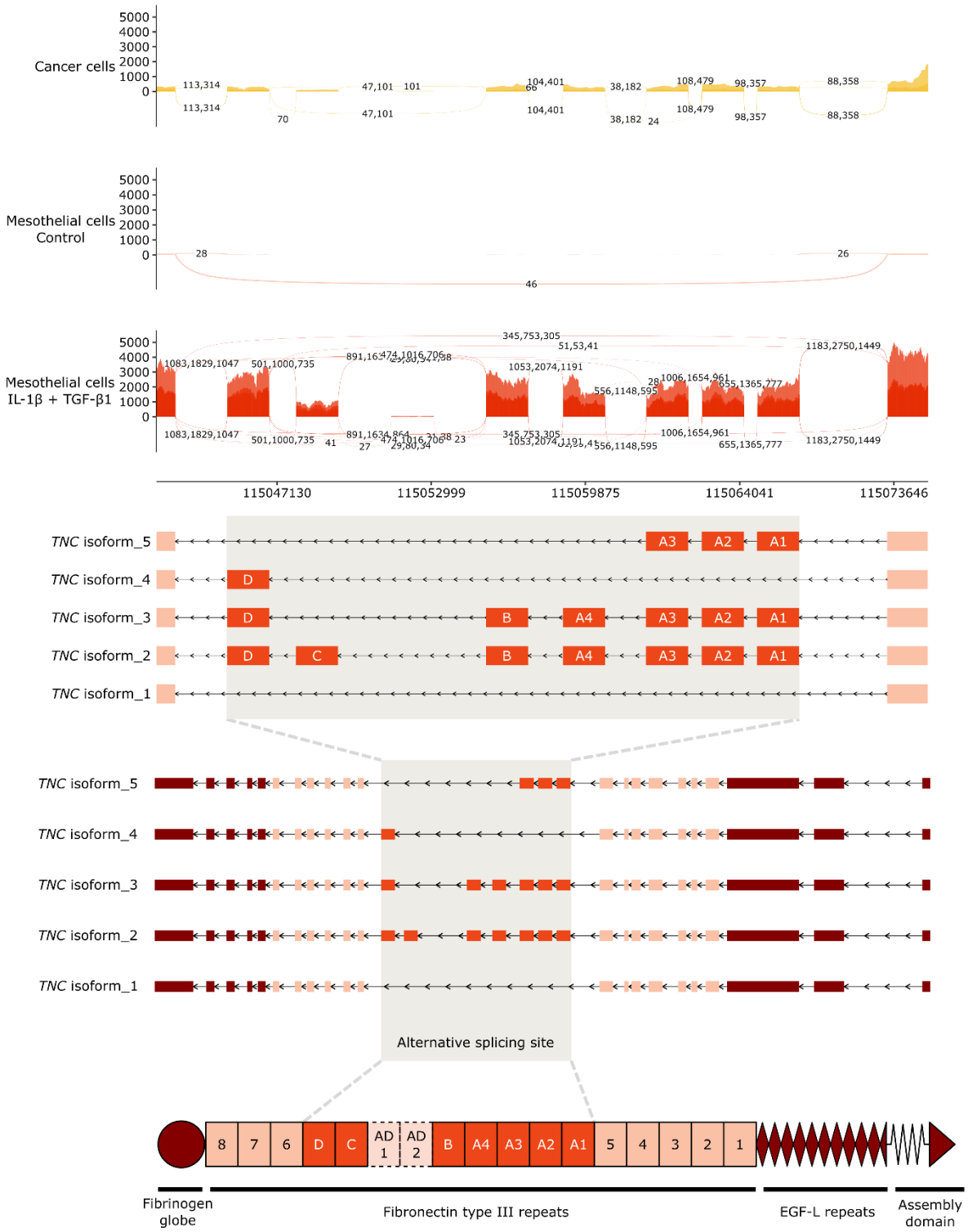
Cancer cells
Mesothelial cells Control
Mesothelial cells IL-1β + TGF-β1
115047130
115052999
115059875
115064041
115073646
TNC isoform_5
TNC isoform_4
TNC isoform_3
TNC isoform_2
TNC isoform_1
Alternative splicing site
8
7
6
D
C
AD 1
AD 2
B
A4
A3
A2
A1
5
4
3
2
1
Fibrinogen globe
Fibronectin type III repeats
EGF-L repeats
Assembly domain

Supplementary Figure 4. TNC isoform analysis in GC tumor cells, mesothelial cells, and MMT-induced mesothelial cells. (Upper part) Sashimi plots for the alternative splicing site in fibronectin type III repeats in the TNC gene of gastric cancer cells, control mesothelial cells and MMT-induced mesothelial cells. (Lower part) Schematic of the alternative splicing pattern in each isoform of TNC. The domain structure of the TNC gene is depicted at the bottom.

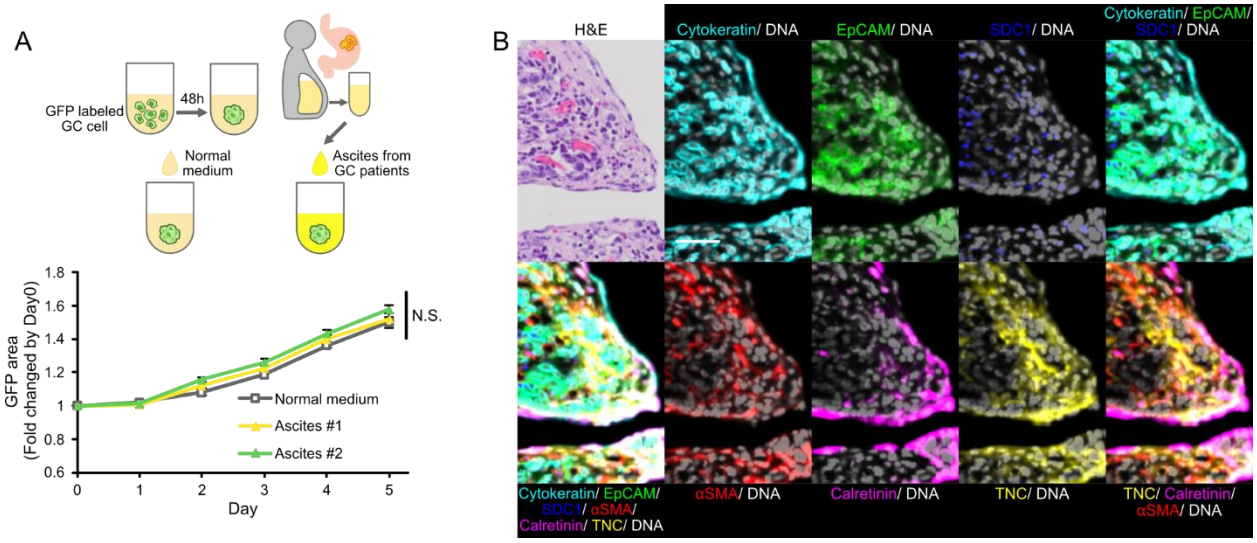

Supplementary Figure 5. Sphere formation assay using GC patient ascites and multiplexed immunohistochemistry analysis of the peritoneal tumor. (**A**) Schematic showing the experimental workflow of the sphere formation assay using normal medium or ascites from GC patients. The growth of colonies in each condition was quantified as the GFP area of colonies normalized to day 0 and is shown in the bottom panel. (**B**) Representative images of hematoxylin-eosin (H&E) staining and fluorescent immunohistochemical staining of cytokeratin, EpCAM, SDC1, αSMA, calretinin, and TNC in the peritoneal disseminating tissue from a GC patient. Scale bar = 50 μm.

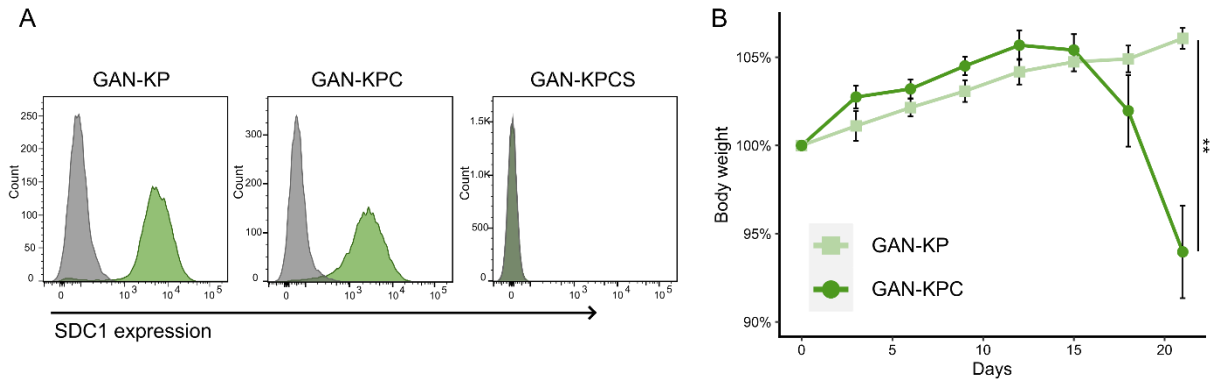

Supplementary Figure 6. Validation of SDC1 expression in GAN-KPCS cells and body weight changes in peritoneal dissemination mouse models. (**A**) Quantification of SDC1 expression in GAN-KP, CAN-KPC, and GAN-KPCS cells by flow cytometry. (**B**) Body weight curves of mice injected with GAN-KP and GAN-KPC cells.